



UPPSALA
UNIVERSITET

*Digital Comprehensive Summaries of Uppsala Dissertations
from the Faculty of Science and Technology 1514*

Modeling and electrical characterization of $\text{Cu}(\text{In}, \text{Ga})\text{Se}_2$ and $\text{Cu}_2\text{ZnSnS}_4$ solar cells

CHRISTOPHER FRISK



ACTA
UNIVERSITATIS
UPSALIENSIS
UPPSALA
2017

ISSN 1651-6214
ISBN 978-91-554-9909-9
urn:nbn:se:uu:diva-320308

Dissertation presented at Uppsala University to be publicly examined in Polhemsalen, Ångströmlaboratoriet, Läderhyddsvägen 1, Uppsala, Thursday, 8 June 2017 at 09:15 for the degree of Doctor of Philosophy. The examination will be conducted in English. Faculty examiner: Professor Janez Krč (University of Ljubljana).

Abstract

Frisk, C. 2017. Modeling and electrical characterization of Cu(In,Ga)Se₂ and Cu₂ZnSnS₄ solar cells. *Digital Comprehensive Summaries of Uppsala Dissertations from the Faculty of Science and Technology* 1514. 86 pp. Uppsala: Acta Universitatis Upsaliensis. ISBN 978-91-554-9909-9.

In this thesis, modeling and electrical characterization have been performed on Cu(In,Ga)Se₂ (CIGS) and Cu₂ZnSnS₄ (CZTS) thin film solar cells, with the aim to investigate potential improvements to power conversion efficiency for respective technology. The modeling was primarily done in SCAPS, and current-voltage (J-V), quantum efficiency (QE) and capacitance-voltage (C-V) were the primary characterization methods. In CIGS, models of a 19.2 % efficient reference device were created by fitting simulations of J-V and QE to corresponding experimental data. Within the models, single and double GGI = Ga/(Ga+In) gradients through the absorber layer were optimized yielding up to 2 % absolute increase in efficiency, compared to the reference models. For CIGS solar cells of this performance level, electron diffusion length (L_n) is comparable to absorber thickness. Thus, increasing GGI towards the back contact acts as passivation and constitutes largest part of the efficiency increase. For further efficiency increase, majority bottlenecks to improve are optical losses and electron lifetime in the CIGS. In a CZTS model of a 6.7 % reference device, bandgap (E_g) fluctuations and interface recombination were shown to be the majority limit to open circuit voltage (V_{oc}), and Shockley-Read-Hall (SRH) recombination limiting L_n and thus being the majority limit to short-circuit current and fill-factor. Combined, E_g fluctuations and interface recombination cause about 10 % absolute loss in efficiency, and SRH recombination about 9 % loss, compared to an ideal system. Part of the V_{oc} -deficit originates from a cliff-type conduction band offset (CBO) between CZTS and the standard CdS buffer layer, and the energy of the dominant recombination path (E_A) is around 1 eV, well below E_g for CZTS. However, it was shown that the CBO could be adjusted and improved with Zn_{1-x}Sn_xO_y buffer layers. Best results gave E_A = 1.36 eV, close to E_g = 1.3-1.35 eV for CZTS as given by photoluminescence, and the V_{oc} -deficit decreased almost 100 mV. Experimentally by varying the absorber layer thickness in CZTS devices, the efficiency saturated at <1 μ m, due to short L_n , expected to be 250-500 nm, and narrow depletion width, commonly of the order 100 nm in in-house CZTS. Doping concentration (N_A) determines depletion width, but is critical to device performance in general. To better estimate N_A with C-V, ZnS and CZTS sandwich structures were created, and in conjunction with simulations it was seen that the capacitance extracted from CZTS is heavily frequency dependent. Moreover, it was shown that C-V characterization of full solar cells may underestimate N_A greatly, meaning that the simple sandwich structure might be preferable in this type of analysis. Finally, a model of the Cu₂ZnSn(S,Se)₄ was created to study the effect of S/(S+Se) gradients, in a similar manner to the GGI gradients in CIGS. With lower E_g and higher mobility for pure selenides, compared to pure sulfides, it was seen that increasing S/(S+Se) towards the back contact improves efficiency with about 1 % absolute, compared to the best ungraded model where S/(S+Se) = 0.25. Minimizing E_g fluctuation in CZTS in conjunction with suitable buffer layers, and improving L_n in all sulfoselenides, are needed to bring these technologies into the commercial realm.

Christopher Frisk, Department of Engineering Sciences, Solid State Electronics, Box 534, Uppsala University, SE-75121 Uppsala, Sweden.

© Christopher Frisk 2017

ISSN 1651-6214

ISBN 978-91-554-9909-9

urn:nbn:se:uu:diva-320308 (<http://urn.kb.se/resolve?urn=urn:nbn:se:uu:diva-320308>)

*To all who supported me and inspired me (and
gave me cookies), but are no longer around.*

List of Papers

This thesis is based on the following papers, which are referred to in the text by their Roman numerals.

- I Frisk, C., Platzer-Björkman, C., Olsson, J., Szaniawski, P., Wätjen, T., Fjällström, V., Salomé, P., Edoff, M., **“Optimizing Ga-profiles for highly efficient Cu(In,Ga)Se₂ thin film solar cells in simple and complex defect models”**, *Journal of Physics D: Applied Physics* 47 (2014), 485104 (12pp)
- II Frisk, C., Ericson, T., Li, S.-Y., Szaniawski, P., Olsson, J., Platzer-Björkman, C., **“Combining strong interface recombination with bandgap narrowing and short diffusion length in Cu₂ZnSnS₄ device modeling”**, *Solar Energy Materials & Solar Cells* 144 (2015), pp 364–370
- III Platzer-Björkman, C., Frisk, C., Larsen, J. K., Ericson, T., Li, S.-Y., Scragg, J. J. S., Keller, J., Larsson, F., Törndahl, T., **“Reduced interface recombination of Cu₂ZnSnS₄ solar cells with atomic layer deposition Zn_{1-x}S_xO buffer layers”**, *Applied Physics Letters* 107 (2015), 243904-1–4
- IV Frisk, C., Ren, Y., Li, S.-Y., Platzer-Björkman, C., **“CZTS solar cell device simulations with varying absorber thickness”**, In proceedings of 2015 IEEE 42nd Photovoltaic Specialist Conference (PVSC), 14-19 June 2015
- V Ren, Y., Scragg, J. J. S., Frisk, C., Larsen, J. K., Li, S.-Y., Platzer-Björkman, C., **“Influence of the Cu₂ZnSnS₄ absorber thickness on thin film solar cells”**, *Physica Status Solidi A* 212 (2015), pp. 2889–2896
- VI Larsen, J. K., Scragg, J. J. S., Frisk, C., Ren, Y., Platzer-Björkman, C., **“Potential of CuS cap to prevent decomposition of Cu₂ZnSnS₄ during annealing”**, *Physica Status Solidi A* 212 (2015), pp. 2843–2849
- VII Frisk, C., Ren, Y., Olsson, J., Törndahl, T., Annoni, F., Platzer-Björkman, C., **“On the extraction of doping concentration from capacitance-voltage: A Cu₂ZnSnS₄ and ZnS sandwich structure”**, submitted (2017)

Reprints were made with permission from the respective publishers.

My contribution to papers

- I Major part of planning, and all the J-V, QE, reflectance and C-V characterization, device modeling and writing with input from co-authors.
- II Major part in planning, all J-V(-T), QE(-V), reflectance, C-V and DCLP characterization, device modeling, and all writing with input from co-authors.
- III J-V-T characterization and input to writing.
- IV Major part in planning, and all device modeling and all writing with input from co-authors.
- V Part in discussion of electrical characterization and theory, minor input to writing.
- VI C-V and DLCP characterization and input to discussion and writing.
- VII Major part in planning, all J-V, C-V, AS characterization, device modeling and writing with input from co-authors.

Related work not included in the thesis

1. Vermang, B., Wätjen, T. J., Frisk, C., Fjällström, V., Rostvall, F., Edoff, E., Salomé, P., Borme, J., Nicoara, N., Sadewasser, S., **“Introduction of Si PERC rear contacting design to boost efficiency of Cu(In,Ga)Se₂ solar cells”**, *IEEE Journal of Photovoltaics* 4 (2014), pp. 1644–1649
2. Vermang, B., Ren, Y., Donzel-Gargand, O., Frisk, C., Joel, J., Salomé, P., Borme, J., Sadewasser, S., Platzer-Björkman, C., Edoff, E., **“Rear surface optimization of Cu₂ZnSnS₄ solar cells by use of a passivation layer with nano-sized point openings”**, *IEEE Journal of Photovoltaics* 6 (2016), pp. 332–336
3. Li, S.-Y., Häggglund, C., Ren, Y., Scragg, J. J. S., Larsen, J. K., Frisk, C., Englund, S., Platzer-Björkman, C., **“Optical properties of reactively sputtered Cu₂ZnSnS₄ solar absorbers determined by spectroscopic ellipsometry and spectrophotometry”**, *Solar Energy Materials & Solar Cells* 149 (2016), pp. 170–178
4. Ericson, T., Larsson, F., Törndahl, T., Frisk, C., Larsen, J. K., Kossyak, V., Häggglund, C., Li, S.-Y., Platzer-Björkman, C., **“Zinc-Tin-Oxide buffer layer and low temperature post annealing resulting in a 9.0 % efficiency Cd-free Cu₂ZnSnS₄ solar cell”**, *Solar RRL* (2017), in press
5. Szaniawski, P., Olsson, J., Frisk, C., Fjällström, V., Ledinek, D., Larsson, F., Zimmermann, U., Edoff, M., **“A systematic study of light-on-bias behavior in Cu(In,Ga)Se₂ solar cells with varying absorber compositions”**, (2017) *IEEE Journal of Photovoltaics* (2017), in press
6. Larsson, F., Shariati Nilsson, N., Keller, J., Frisk, C., Kossyak, V., Edoff, M., Törndahl, T., **“Record 1.0 V open-circuit voltage in wide band gap chalcopyrite solar cells”**, submitted (2017)
7. Bras, P., Frisk, C., Tempez, A., Niemi, E., Platzer-Björkman, C., **“Ga-grading and SCAPS simulation of an industrial Cu(In,Ga)Se₂ solar cell produced by an in-line vacuum, all-sputtering process”**, submitted (2017)

Contents

1. Introduction.....	13
2. Theory of semiconductor solar cells	17
2.1 Photovoltaic effect.....	17
2.2 P-n junction and basic equations	18
2.3 Carrier concentrations and the Fermi level	21
2.4 Limitations and loss mechanisms.....	22
3. Thin film solar cells	24
3.1 Cu(In,Ga)Se ₂ (CIGS).....	26
3.2 Cu ₂ ZnSnS ₄ (CZTS)	27
4. Device characterization.....	29
4.1 Standard test conditions.....	29
4.2 Current-voltage.....	30
4.2.1 Diode model.....	32
4.2.2 Parameter extraction	34
4.2.3 Temperature variation.....	35
4.3 Quantum efficiency	37
4.3.1 Internal quantum efficiency	37
4.3.2 Voltage dependent quantum efficiency	38
4.3.3 Bandgap extraction	39
4.4 Admittance spectroscopy	40
4.4.1 Temperature variation.....	42
4.5 Capacitance-voltage	42
4.5.1 Measurement frequency.....	42
4.5.2 Doping concentration.....	43
5. Device modeling and simulations	45
5.1 SCAPS-1D	45
5.1.1 Input parameters	46
5.1.2 Creating a model.....	46
5.2 Simulations.....	47
5.2.1 Current-voltage.....	48
5.2.2 Quantum efficiency	48
5.2.3 Capacitance-voltage.....	48

6. Results and discussions	49
6.2 Ga-profile optimization in CIGS	49
6.2 Bottlenecks in high efficiency CIGS devices	53
6.3 Absorption coefficient and bandgap narrowing in CZTS	55
6.4 Reduction of interface recombination in CZTS	56
6.5 Collection length and doping concentration in CZTS	57
6.6 Prospect of sulfo-selenium grading in CZTS	61
7. Concluding remarks and outlook	67
Sammanfattning på svenska	70
Acknowledgements	74
Appendix A	77
A.1 Loading large sets of data from J/C-V-T	77
A.2 Temperature dependent current-voltage analysis in MATLAB	78
A.3 Temperature dependent admittance spectroscopy analysis in MATLAB	79
References	80

Abbreviations and acronyms

ac	Alternating current
ALD	Atomic layer deposition
AM1.5G	Air mass 1.5 global
AS	Admittance spectroscopy
c-Si	Crystalline silicon
C-V	Capacitance-voltage
CBO	Conduction band offset
CZTS	$\text{Cu}_2\text{ZnSnS}_4$
CZTSe	$\text{Cu}_2\text{ZnSnSe}_4$
CZTSSe	$\text{Cu}_2\text{ZnSn}(\text{S},\text{Se})_4$
dc	Direct current
DG	Double graded
E-PBT	Energy payback time
EPS	Energy-dispersive X-ray spectroscopy
GD-OES	Glow discharge optical emission spectroscopy
GGI	Ga/(Ga+In)
IR	Infrared
IQE	Internal quantum efficiency
J-V	Current-voltage
J-V-T	Temperature dependent current-voltage
MIS	Metal-insulator-semiconductor
PBT	Payback time
PDT	Post-deposition treatment
PL	Photoluminescence
PV	Photovoltaic
QE	Quantum efficiency
QE-V	Voltage dependent quantum efficiency
R-T	Reflectance-transmission
S/VI	$\text{S}/(\text{S}+\text{Se})$
SCAPS	Solar cell capacitance simulator
SCR	Space charge region

SG	Single graded
SLG	Soda lime glass
SRH	Shockley-Read-Hall
STC	Standard test conditions
TCO	Transparent conductive oxide
UV	Ultraviolet
XRD	X-ray diffraction
ZTO	$\text{Zn}_{1-x}\text{Sn}_x\text{O}$

1. Introduction

One of the pillars of the modern and growing society is electrical energy. It is a commodity that, thanks to technology, can enable almost any process, whether it is information exchange, or the refinement, production or recycling of other resources. Any task executed by electronics is dependent on electrical energy, and it is hard to imagine a world without electronic devices surrounding us. Therefore, the production and availability of electrical energy, especially in developing countries, should be given high priority, and for a sustainable society within a foreseeable future, focus should be clean production. With production of electrical energy, there is no “one solution fits all”. Instead, many different technologies compete to find their respective appropriate place, but there is strength in versatility and security in redundancy. Largely untapped is the potential from solar irradiation, the yearly global average being around 180 W m^{-2} at the surface of the Earth, which equals around $80 \times 10^9 \text{ TWh}$, or approximately $69 \times 10^7 \text{ Mtoe}^1$ over the course of a year [1]. As important as the sun has been for the evolution of life, the irradiation it provides is still an under-used commodity by the modern society: The Earth is exposed to solar irradiance equal to more than 7 000 times the global energy consumption, which in 2014 was 9 425 Mtoe [2]. Thus, utilizing only a fraction of the solar irradiance can still lead to vast improvements in living standards. Harvest of the energy from the sun can take different forms, but the most elegant form is by use of solar cells, i.e. photovoltaics (PV)². With the PV effect, the solar irradiation is directly converted into electrical energy, and for a conventional semiconductor PV module there are no moving parts. As such the lifetime of solar cells can be very long [3, 4].

Research on solar cells started already in the 19th century with Becquerel discovering the PV effect with an electrochemical cell [5]. The first study published on a solid state device, of which most modern solar cell technologies are based, was done in 1877 [6]. In the middle of the 1880s, the very first solar panels, based on gold coated on selenium, or the Fritts cells [7], were demonstrated by Charles Fritts on a rooftop in New York City, see figure 1. Unfortunately, the work was overshadowed (not literally!) by the first coal power plant constructed by Edison Illumination

¹ Megaton oil equivalent.

² At least according to some of the scientists doing research on solar cells.



Figure 1. The very first solar panels on a rooftop in New York City (1880's) [8], made from gold coated on selenium, by Charles Fritts [7]. As it turned out this was a great idea, even if the efficiency probably was abysmal. Can be compared with modern installations, e.g. the one shown in figure 2.

Company with none other than Thomas Edison at the helm. It was not until the middle of the 20th century that solar cells became a hot topic, particularly after the invention of the silicon (Si) solar cell by Bell Labs [9] with around 6 % energy conversion efficiency. Since then, Si PV has been the dominant technology, and other technologies have been used in niche applications [10]. In the late 1970s the first thin film solar cells were developed for use in calculators, based on amorphous Si with efficiency below 5 %. Since the beginning of the 1980s, thin film technologies have been catching up to standard crystalline-Si (c-Si) technology, and two thin film technologies in particular are entering the commercial realm: cadmium-telluride (CdTe) and copper-indium-gallium-selenide (Cu(In,Ga)Se_2 , or CIGS)³. At the time of writing, CdTe have reached lab-record efficiency of 21.1 %, attributed to First Solar [11], and CIGS have reached lab-record efficiency 22.6 %, attributed to the Centre for Solar Energy and Hydrogen Research Baden-Württemberg [12]. For the efficiency development of these and other PV technologies over the course of history, the National Renewable Energy Laboratory publishes an updated lab-scale efficiency chart yearly [13], and the official records, with a minimum of 1 cm^{-2} scale devices, are presented by Green et al. [14]. For a rundown of a 6000 year history of solar energy and solar cells, see *Let it Shine* by Perlin [15].

³ The names of the technologies are derived from the absorber layer, i.e. the most active part of the PV device.

All thin film technologies share the trait that the absorption of light is much more efficient than in c-Si technology. It means that the absorber layer can be made much thinner, and thus; the categorization. While c-Si absorber layers are thin by most standards; a few hundred μm , putting it conveniently between the thickness of a human hair and a flea that might inhabit it; the thin film absorber layer thickness is around $1\ \mu\text{m}$, equivalent to only a fraction of the thickness of a human hair, and practically invisible to the flea. The benefit is lower production cost due to less material, time, and energy consumption required in the fabrication process. In addition; thin films enable solid state devices to be made flexible, if it can be deposited on a flexible substrate [16]. In the end, it comes down to how commercially competitive the end product in the form of a PV module can be. Unless made for niche applications, the most important benchmark of a PV module is the output power per invested amount of money, or Watts peak power per dollar, which is now down to below $0.5\ \text{W}_\text{p}/\$$ [10]. In principle, one can measure the feasibility of a PV module by energy payback time (E-PBT), which is an estimate of how fast the PV module can produce the amount of energy required to produce the module itself, under nominal conditions. The E-PBT is much shorter than the monetary PBT for the end-consumer, and on average E-PBT is shorter for thin film solar cells than c-Si PV by approximately a factor of two [17]. For these reasons efficiency is the major property of interest, for end-consumers and researchers alike, since it will affect any PBT.

In this thesis, research in the form of device characterization and modeling has been done on CIGS and its sibling-technology $\text{Cu}_2\text{ZnSnS}_4$ (CZTS) thin film solar cells. CZTS consists of only abundant elements which may factor into pricing for future large scale PV production since scarce elements, such as In, are more price-sensitive to the market [18]. Evident from the previous paragraph, the long-term goal is to increase the efficiency. By using device modeling and (opto-)electrical device characterization to further our understanding, we are incrementally moving towards that goal.

So why modeling, and what is it? In short, modeling is a useful tool to bridge between theory and experiment. The thin film solar cells have a complexity due to the multitude of materials used, but it does not deter us from trying to understand them. When characterizing the devices one has to apply physical models in order to make sense of the data. However, if approached analytically, one usually has to resort to approximations to get a solution, and when these approximations do not apply, modeling becomes quite handy [19]: Instead of approximating the system with analytically solvable equations, the exact equations can be solved numerically to a point where the solution converges within a limit of error acceptable to the user. The structure in the system is represented by a discreet mesh, in which each point in the mesh is considered homogenous in all physical parameters, and for which each point is coupled with its own set of equations. Thus, the limit is

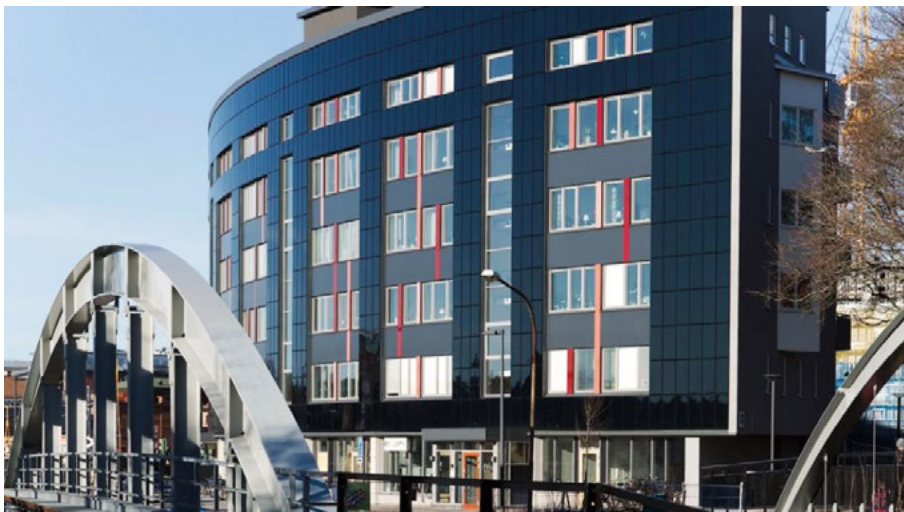


Figure 2. A modern way of incorporating solar cells into buildings, Uppsala City. The black façade are thin film PV modules made by Solibro GmbH, a spin-off company originally formed from the thin film solar cell group at Ångström, Uppsala University. Picture by Skanska AB.

set by computational power, and not by approximations of the theory. Letting the computer do the heavy lifting means more time for other work, or maybe a workout with some heavy lifting on our own. But with more computational power comes the need for more electrical power, and so the cycle continues...

The aim of this thesis is to study both the possibility to enhance performance of the mature CIGS PV technology, see paper I, and study the dominating loss mechanisms in the newer CZTS technology, with an overview in paper II, and on individual parts in paper II, III, IV, V and VI. In addition, since device characterization has been such an integral part of this thesis, in-depth analyses have been conducted on how to better utilize and obtain useful and trustworthy results from device characterization, see paper II and VII. Naturally, focus of the discussions has been on how the CIGS and CZTS absorber layers, including their interfaces, affect device properties and performances. The aim of this summary is to describe, in a pedagogical way, the general theory of the photovoltaics, see chapter 2, the CIGS and CZTS thin film photovoltaic structures and layer properties, see chapter 3, an extensive description of the key opto-electrical device characterization methods, and modeling, simulation and numerical analyzation methods, see chapter 4 and 5. Key results from the papers as well as complementary and unpublished results are discussed in chapter 6, and conclusions with an outlook can be found in chapter 7.

2. Theory of semiconductor solar cells

This chapter is dedicated to the fundamental theory of solar cells, including the basic semiconductor physics required to model a solar cell. Additional theory related the characterization of solar cells is presented for respective technique in chapter 4.

2.1 Photovoltaic effect

The PV effect, first observed by Becquerel in 1839 [5], is the conversion of electromagnetic radiation, i.e. light, directly into electrical energy. However, it was not until Einstein explained his thoughts on light that the photoelectric and PV effect could be readily understood [20]. According to the principles of wave-particle duality of quantum mechanics, the light is composed of discrete energy quanta called photons, each photon with energy (E) that depends on its wavelength (λ)

$$E = hc/\lambda \quad (1)$$

where h is Planck's constant and c is the speed of light. In PV research, E is commonly given in the unit eV, and λ in the unit nm, and with these units (1) can be re-written as $E \approx 1240/\lambda$. The energy 1 eV equals one elemental charge $q = 1.6 \times 10^{-19}$ C at a potential $V = 1$ V.

A typical solar cell is made from semiconductor materials, which per definition have an energy gap between its outermost filled electronic states at energy E_V , and the next set of available empty states at energy E_C , see figure 3. The outer filled states are occupied by valence electrons that form the electronic bonds in the material, and these states make up the valence band. The absence of electrons in the valence band are called holes, which are quasiparticles with $+q$ charge. The available empty states at higher energies above the gap is known as the conduction band. Electrons that inhabit the conduction band are delocalized and move freely in the material, carrying the charge $-q$. The energy gap between the two bands is called the bandgap (E_g). When photons with energy larger than E_g are absorbed in a semiconductor, their energy is converted into the excitation of electrons, moving the electrons from the valence to the conduction band and leaving holes behind, and thus creating electron-hole pairs. Typically, electron-hole pairs recom-

bine, giving up their energy in form of light and/or heat. To instead utilize the electron-hole pair generation in form of electrical energy, it is important to separate the electron from the hole before they can recombine. A successful separation means an increase in net charge carrier concentration difference, i.e. a potential difference. If connected to an external load, a current will pass through the circuit to make electrical work before the charges can reunite. In a semiconductor solar cell, the electron-hole separation takes place in the so called p-n junction – by far the most important feature of the whole device.

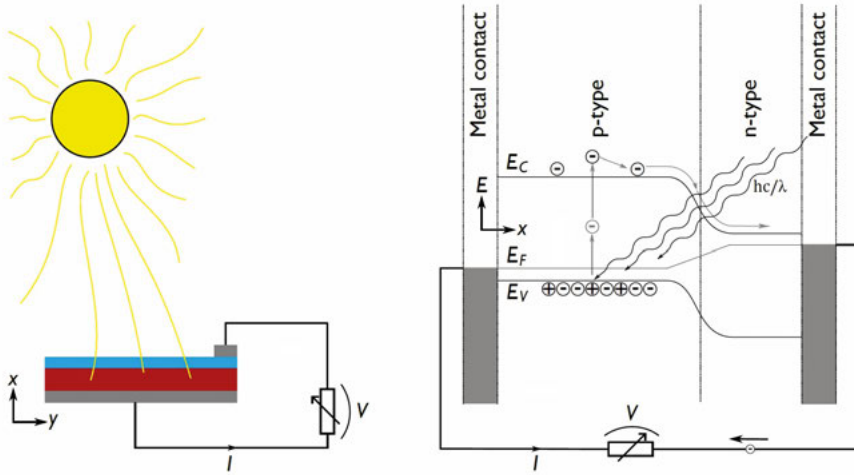


Figure 3. The PV effect. Electrons are excited from the valence band to the conduction band, made freely available, and then collected by the p-n junction. Per definition, the direction of the current is in the opposite direction of the electrons. The red color represents a p-type absorber layer, and the blue the n-type front layers. The concept of p- and n-type semiconductors will be discussed in section 2.2, and the Fermi level E_F will be discussed in section 2.3. Re-created from [21].

2.2 P-n junction and basic equations

P-type semiconductors are defined by hole majority charge carriers and are created with defects⁴ that accept (N_A) electrons from the valence band, thus doping it with holes (p). N-type doping is achieved with defects that donate (N_D) electrons (n) to the conduction band. The p-n junction is formed when a p-type and n-type semiconductors come in contact. Although each semiconductor is electrically neutral, the difference in majority charge carrier concentrations will initiate a diffusion process. The electrons on the n-type side will diffuse into the p-type side to occupy the state that was previously

⁴ In thin film technology, these defects are intrinsic, see chapter 3. In c-Si technology, these defects are intentionally added and commonly referred to as dopants instead of defects.

occupied by a hole, and vice versa. As a charge carrier is moving from one semiconductor type to another, it will change the charge balance in the so-called space charge region (SCR), which becomes depleted of free charge carriers. The new charge balance in the SCR cause an electrical field from the n-type (now positively charged donor defects) to the p-type (negatively charged acceptor defects) semiconductor. In the field, free charge carriers will be promoted (drifting) in one way, and opposed in the other way, depending on their charge. Thus, there will be two competing forces in the p-n junction, diffusion opposed by drift. Moving charges means electric current, and the hole current density J_h and electron current density J_e each consist of a drift and diffusion part;

$$J_p = q(\mu_p \mathbf{p} \cdot \boldsymbol{\xi} - D_p \nabla \cdot \mathbf{p}), J_n = q(\mu_n \mathbf{n} \cdot \boldsymbol{\xi} + D_n \nabla \cdot \mathbf{n}) \quad (2)$$

and total current density $J_{tot} = J_p + J_n$. In equilibrium $J_{tot} = 0$. The drift current densities are proportional to the electric field $\boldsymbol{\xi}$, the mobility μ , and the carrier concentrations p and n . The diffusion current densities are proportional to the carrier concentration gradients and the diffusion constant (D). The mobility and diffusion constant are related via the Nernst-Einstein equation;

$$D = \frac{\mu k_B T}{q}, \quad (3)$$

where k_B is Boltzmann's constant and T is the temperature. The SCR is also referred to as depletion region due the low concentration of free charge carriers that, if present, will be swept away by the electrical field. The depletion width is denominated W_D . If the total charge concentration ρ in a structure is known, including fixed and free charge, one can use Poisson's equation of electrostatics,

$$-\nabla^2 \psi = \nabla \cdot \boldsymbol{\xi} = \frac{\rho}{\epsilon}, \quad (4)$$

to calculate the built in electrical field $\boldsymbol{\xi}$ and potential ψ , where ϵ is the dielectric permittivity. Figure 4 depicts Poisson's equation solved for a simple abrupt p-n junction in 1-D. For any given volume in the structure, it follows from continuity (charge conservation) that, at steady state,

$$\nabla \cdot \mathbf{J} = q(G - U), \quad (5)$$

where U is the net recombination rate, and G is the net generation rate. Relationship (2), (4) and (5) are the fundamental semiconductor physics equations and form the basis for any solar cell device modeling.

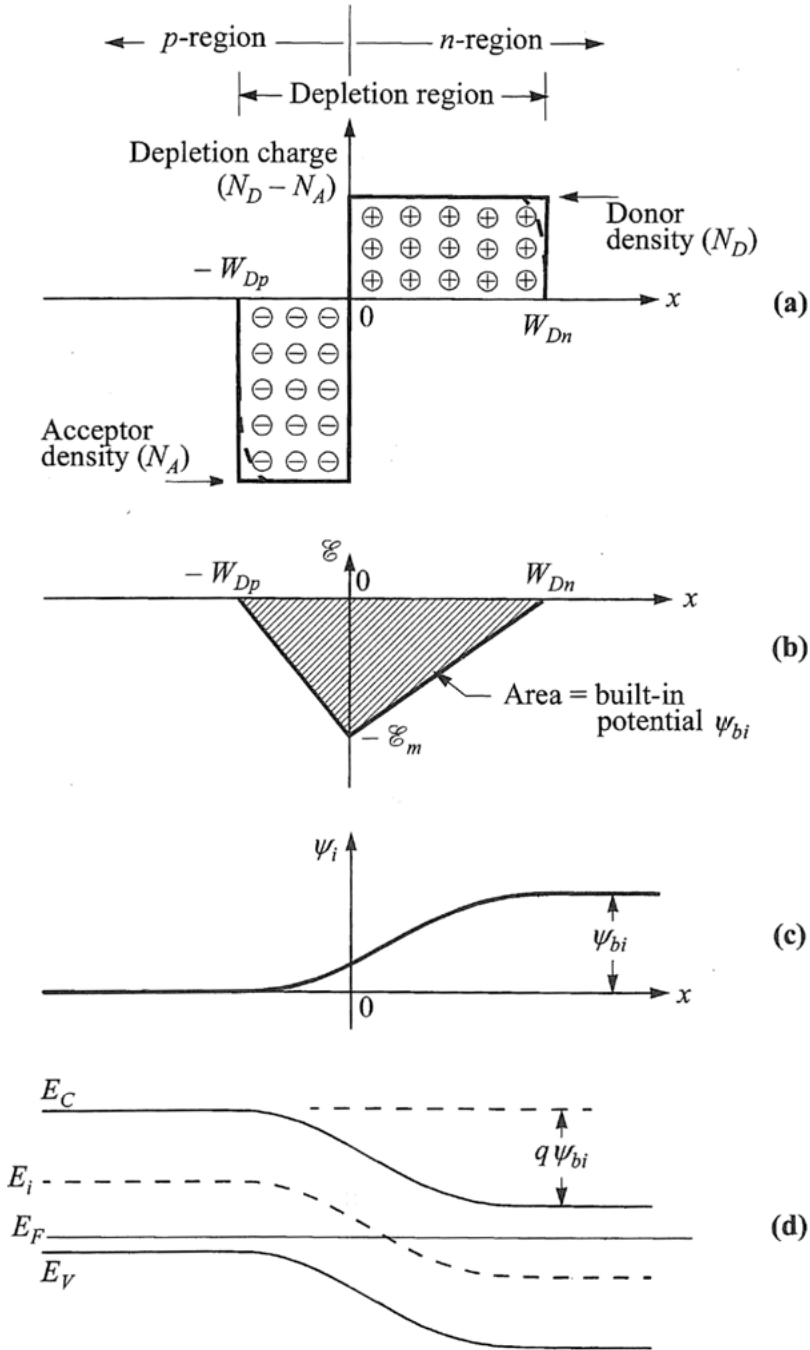


Figure 4. The solution to Poisson's equation (4) in graphical format for an abrupt p-n junction. Figure re-created with permission from John Wiley and Sons [22]. (a) depicts the charge distribution, (b) the electric field, (c) the potential and (d) the effect on the band diagram of a p-n homojunction.

2.3 Carrier concentrations and the Fermi level

Introducing Fermi-Dirac statistics, the probability of finding a free charge carrier at energy E is described by the Fermi function

$$F(E) = \frac{1}{1 + \exp[(E - E_F)/k_B T]}, \quad (6)$$

where E_F is the Fermi level, a quantity defined as the energy at which there is a 50 % probability of finding a free charge carrier. T is the absolute temperature which defines the edge of the probability curve. At 0 K the Fermi function becomes a step function, whereas at higher temperature the step is smeared out due to thermal excitation of electrons from the valence band to the conduction band. The effectiveness of thermal excitation depends on the semiconductor, which will have a certain density of states (DOS) for each of the energy bands. Close to the band edges, where most of the action takes place, one can approximate the DOS with an effective DOS; N_V^* for the valence band and N_C^* for the conduction band. The free charge carriers are then

$$n = N_C^* \exp[(E_C - E_F)/k_B T], \quad p = N_V^* \exp[(E_F - E_V)/k_B T] \quad (7)$$

where $E_{C,V}$ is the band edge energy of respective band. An intrinsic semiconductor, ideally without defects, will per definition have a total concentration of electrons and holes such that $n = p$, and where $E_F = E_i \approx E_g/2$, if $N_V^* \approx N_C^*$. The intrinsic carrier concentration, in equilibrium conditions, is defined

$$n_i \equiv \sqrt{np} \quad (8)$$

and consequently,

$$n_i^2 = N_V^* N_C^* \exp(-E_g/k_B T). \quad (9)$$

For a semiconductor with defects in the form of either intentional doping or intrinsic doping, $n \neq p$, but eq. (8) and (9) still apply. In this case, to maintain charge neutrality,

$$p + N_D^+ = n + N_A^-. \quad (10)$$

In non-equilibrium conditions, however, such as with a voltage bias or illumination of light;

$$n_i^2 \neq np. \quad (11)$$

In such a case, the Fermi level is divided into the quasi Fermi levels of holes and electrons, E_{Fp} and E_{Fn} . The positions of the quasi Fermi levels, E_{Fp} relative E_V , and E_{Fn} relative to E_C , still determines the concentration of respective species, with the quasi Fermi levels replacing E_F in (7).

2.4 Limitations and loss mechanisms

The theoretical upper limit for the power conversion efficiency of a solar cell was first calculated by Shockley and Queisser for an ideal system [23], using the detailed balance principle. Here, one considers the trade-off between generation and thermalization losses with a single bandgap material, as well as radiative recombination which must exist because of thermal equilibration. Generation losses are the losses due to insufficient energy in the light, when E from equation (1) is lower than E_g , and thermalization losses for $E > E_g$ is caused by the extra energy dissipating as heat. Originally, the Shockley-Queisser limit was calculated assuming the solar radiation being equivalent to a 6000 K black body radiation, and the optimum single bandgap energy was found to be around 1.1 eV, giving slightly more than 30 % efficiency. However, depending on the spectra used, one finds different optimum bandgaps between 1.1 and 1.4 eV, always slightly above 30 % efficiency. In practice, however, one needs to consider a multitude of other losses that arise from imperfect materials or interfaces between materials, that reduces the power conversion efficiency; additional recombination including defect assisted recombination that follows the Shockley-Read-Hall (SRH) formalism, and Auger recombination for highly doped semiconductors; optical losses including reflectance, parasitic absorption and incomplete absorption; and resistive losses including series resistance and shunt conductance. A figure illustrating current-reducing mechanisms can be found in chapter 4 (figure 11). The recombination loss mechanisms and their influence on device performance were central in paper II. In thin films, SRH recombination plays an important role, and the SRH recombination rate is given by

$$U = \frac{\sigma_n \sigma_p v_{th} N_T (np - n_i^2)}{\sigma_n \left[n + n_i \exp\left(\frac{E_T - E_i}{kT}\right) \right] + \sigma_p \left[p + n_i \exp\left(\frac{E_i - E_T}{kT}\right) \right]}, \quad (12)$$

and as a rule of thumb any recombination rate is proportional to the number of total free carries

$$U \propto np - n_i^2. \quad (13)$$

In the SRH formalism (12), σ are capture cross-sections, and v_{th} is thermal velocity, N_T and E_T are defect concentration and energy level above the valence band, respectively. It is important to note that the recombination pathways are seldom saturated, thus, they interdependently facilitate recombination in order of effectiveness and accessibility to the charge carriers. To get exact results it is highly beneficial to use a modeling tool to plot the actual recombination currents.

An important characteristic, used throughout this thesis and related papers, is minority carrier diffusion length L which is related to U via the minority carrier lifetime (e.g. electrons for a p-type semiconductor)

$$\tau_n = \Delta n U^{-1} \quad (14)$$

such that

$$L_n = \sqrt{D_n \tau_n}. \quad (15)$$

Statistically, there is approximately a 37 % probability for a carrier to travel the full length of L without any external perturbation. Together with the width of the SCR, the diffusion length determines the efficiency of collection of minority carriers, and the importance of this is discussed in detail in paper II, IV and V. Additional theory of semiconductor device physics is well described by Sze and Ng [22], and specific PV physics, by Green [24]. Additional theory relevant for this thesis can be found in chapter 4, coupled with the characterization techniques.

3. Thin film solar cells

Thin film solar cells are all based on direct bandgap semiconductor materials, where the probability of absorption is far larger than for indirect bandgap materials such as c-Si PV [24]. As a consequence, absorber layers with thickness of the order of 1 μm is enough to absorb most of the light, while c-Si PV requires two order of magnitude thicker absorber layers. In addition to the benefits of processing a thin layer, it also puts less requirement on the mobility (3) and lifetime (14) of minority carriers in the absorber layer, since the carriers need to travel a shorter distance to be collected. The most basic structure needed to make a thin film device is, in order from substrate to the front of the device; a back contact (commonly a metal); the absorber layer itself; a front layer to collect and conduct the charge carriers (with opposite doping as compared to the absorber layer). The front is commonly a transparent conductive oxide (TCO).

In practice, the use of a substrate is needed for structural purposes, and the substrate can be anything from polymers to metals or glass. Commonly, non-flexible ordinary soda-lime glass (SLG) has been used as a substrate since it was reported to make CIGS more efficient in 1993, compared to borosilicate glass, sapphire, and sintered alumina [25]. The enhanced efficiency with SLG is due to the diffusion of Na. Heavier alkali metals, incorporated with post-deposition treatments (PDT), have been shown to improve the performance of CIGS even further [26, 27]. Alkali metals in CZTS have also been shown to various degrees to increase p-type doping concentration by passivation of compensational donors [28, 29], as well as enhance grain size [28, 30-32] and improve device performance [28, 32]. For alternative substrates, a sodium containing precursor can be deposited before the absorber deposition, having similar beneficial effects to those of SLG [33, 34].

Thin film absorber layers themselves have intrinsic defects that are material and process dependent, in part due to alkali metals, but the major influence comes from the absorber composition. In the end, for viable chalcogen-rich and Cu-poor processes, CIGS and CZTS turn out as p-type. Consequently, in contrast to the conventional p- and n-type Si homojunction, the n-doped side in a thin film solar cell is fabricated by using another semiconductor, forming a heterojunction with the absorber, see figure 5. This puts high requirements on the n-type semiconductor [35], and the standard TCO ZnO:Al does not form a good heterojunction. As such, a buffer layer is introduced; if crystalline then it should preferably have matching lattice con-

stant. Moreover, it should not form a negative conduction band offset (CBO) since this may limit V_{OC} due to the limitation of quasi Fermi level splitting. Experimentally, in a study on CIGS with $Zn_{1-x}Mg_xO$ buffer layers, a positive CBO around 0.3 eV was found to give highest efficiency [36]. Simulations generally agree on a beneficial effect from moderately positive CBO, around 0 – 0.4 eV [37, 38], depending on the parameters set. Having inversion at the interface to create a buried homo-junction can decrease interface recombination in the presence of interface traps. It should be noted that with process conditions to form an average positive CBO instead of perfect line-up, the probability of forming a negative CBO is reduced⁵, and a small positive CBO will not block the light current substantially. Optically, the buffer layer should be transparent if no collection of carriers is possible from the n-type semiconductor.

Although main focus in this thesis has been on the absorber layers, it should be emphasized that a lot of work in general goes into improving the buffer and front stack, e.g. by using non-toxic elements with well-matched CBO, and having a high mobility type TCO to reduce free carrier absorption [35, 39, 40].

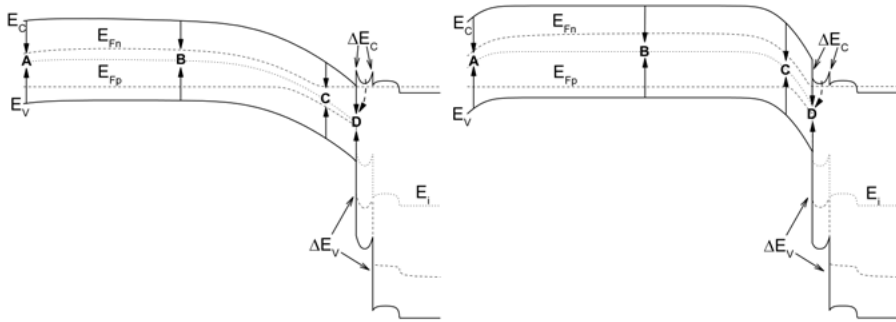


Figure 5. The band diagrams of CIGS (left hand side) and CZTS (right hand side) thin film solar cells. Recombination pathways are marked and based on models used in paper I and II. (A) marks back contact recombination, (B) neutral bulk recombination, (C) recombination in the SCR, and (D) interface recombination. Notice the difference between the models, in bandgap magnitude and grading, as well as CBO difference at the interface between absorber and buffer layer. In addition, the CZTS model has higher doping concentration compared to the CIGS model, which manifests as a sharper band bending in the heterojunction.

⁵ Experimental uncertainty in the fabrication process may cause lateral surface variation, and coupled with the uncertainty in the X-ray photoelectron spectroscopy and quantum efficiency used in [37] it may be better to “be on the safe side”.

3.1 Cu(In,Ga)Se₂ (CIGS)

CIGS is a chalcogenide that forms chalcopyrite crystal structure. Record efficiency of CIGS thin film solar cells is close to 23 % for lab-scale devices [12], and the record efficiency for a $30 \times 30 \text{ cm}^2$ sub-module is 19.2 % [41]. The standard stack is made up of SLG substrates, a Mo back contact, CIGS absorber layer, CdS buffer layer and i-ZnO and ZnO:Al transparent front contact. In figure 6, a transmission electron microscopy image shows the cross-section of such a device. The CIGS is made non-stoichiometric, usually Cu-poor with the ratio of Cu over the type-III elements in the periodic table; $\text{Cu/III} \approx 0.9$. In addition CIGS is commonly fabricated in Se-rich conditions to avoid loss of Se. The final stoichiometry heavily influences the defects of the material [42]. In-house CIGS are made with a static or in-line co-evaporation system, and the process of the complete device fabrication can be found in reference [43]. The improvement of efficiency in CIGS technology in the 1980's and 1990's have been well summarized [44]. The largest factor of efficiency improvement over the years has been the engineering of the absorber layer itself. Well controlled growth conditions are imperative to good CIGS crystal quality, and intentional variation of the growth parameters allows achieving compositional gradients throughout the films. With the ratio $\text{GGI} = \text{Ga}/(\text{In}+\text{Ga})$ one can effectively tune the bandgap and electron affinity of CIGS [45], making it possible to tailor the absorption, collection and junction properties with a so-called Ga-profile, where [46];

$$E_g = 1.01 + 0.626 \times \text{GGI} - 0.167 \times \text{GGI}(1 - \text{GGI}) \quad [\text{eV}] \quad (16)$$

In other words, one can tune the bandgap between approximately 1 eV and 1.6 eV. Paper I goes in depth of the utilization and tuning of the Ga-profile, for CIGS devices with efficiencies above 19 %.

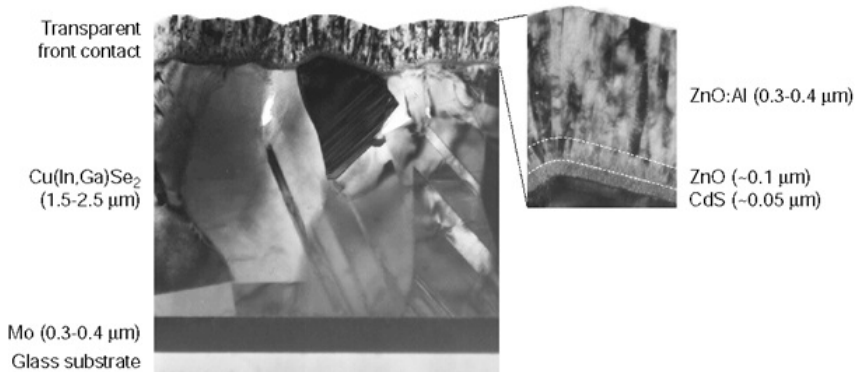


Figure 6. Cross-section transmission electron micrograph of a standard CIGS solar cell stack.

3.2 Cu₂ZnSnS₄ (CZTS)

CZTS is a chalcogenide that forms the kesterite crystal structure⁶. The idea of CZTS comes from replacing the type III elements in CIGS with more commonly available elements, such as Zn and Sn [18]. Consequently, CZTS and its derivatives share a lot with the CIGS technology, including good optical properties [47], and it is possible to utilize the standard front stack for a fully functional device. Ongoing research is investigating whether, and to what extent, the traditional CdS buffer layer should be replaced for CZTS, e.g. with Zn(O,S) [48] or Zn_{1-x}Sn_xO (ZTO) [39, 49], the latter being the topic of paper III. Record efficiency is currently held with CdS buffer layers; 12.6 % [50, 51] attributed to Solar Frontier and IBM, for a hydrazine solution based deposition process with a mix of Se and S (CZTSSe). For a pure sulfide CZTS device the record efficiency is 9.5 % attributed to University of New South Wales [52]. There is still a large potential for further improvement to kesterites, and the mechanisms limiting efficiency have been discussed in references [53-58], and is the main topic of paper II. The in-house CZTS layer is fabricated with precursor sputtering from compound targets or reactive sputtering with H₂S from metal targets, followed by an anneal step to crystalize the film. In figure 7, the scanning electron microscopy top and cross-section views before and after annealing can be seen. For a detailed description of the absorber deposition process, please see [48] and paper V. Most work on in-house CZTS absorbers has been on pure-sulfides, but a sulfo-selenide procedure has also been established [59]. In a similar manner to GGI engineering in CIGS, a variation of the ratio $S/VI = S/(S+Se)$ allows for a tunable bandgap that may vary between approximately 1 eV for $S/VI = 0$ [60, 61] and around 1.5 eV for $S/VI = 1$ [61-63].

The CZTS film is intentionally made non-stoichiometric in a similar manner to CIGS, commonly with $Cu/Sn = 1.9-2.0$ and $Zn/(Cu+Sn) \approx 0.4$. Non-stoichiometry in CZTS will naturally induce intrinsic defects, in addition to segregation of secondary phases, which in turn may lead to complex material characteristics. Depending on the nature of the non-stoichiometry, the CZTS can be categorized into different single phase types, A, B, C... etc. [64]. These types are best described by a phase diagram, where, in addition, the most probable secondary phases can be predicted. In our baseline CZTS process type A (Cu-poor and Zn-rich) and type B (additionally Sn-poor) are formed. In these types, one expects defect complexes such as $[Cu_{Zn}^- + Zn_{Cu}^+]$, $[V_{Cu}^- + Zn_{Cu}^+]$ and $[2Zn_{Cu}^+ + Zn_{Sn}^{2-}]$ to form [65, 66]. The $[Cu_{Zn}^- + Zn_{Cu}^+]$ defect complex is theorized to form in clusters, effectively causing a bandgap and electrostatic fluctuation that may limit the performance of CZTS devices [67]. In fact, the “real” bandgap energy of CZTS is an ambiguous property that is difficult to define experimentally, since it will vary with composition,

⁶ It has been debated whether or not CZTS forms a stannite structure, but recent research points towards kesterite being of lower formation energy, e.g. [108].

disorder and defect complexes, as well as measurement method. While most optical measurements and theoretical calculations end up around 1.5 – 1.6 eV, photoluminescence (PL) have shown the main peak of CZTS slightly over 1.3 eV [68], see paper II and III. A review on the kesterites and its challenges can be found in [69].

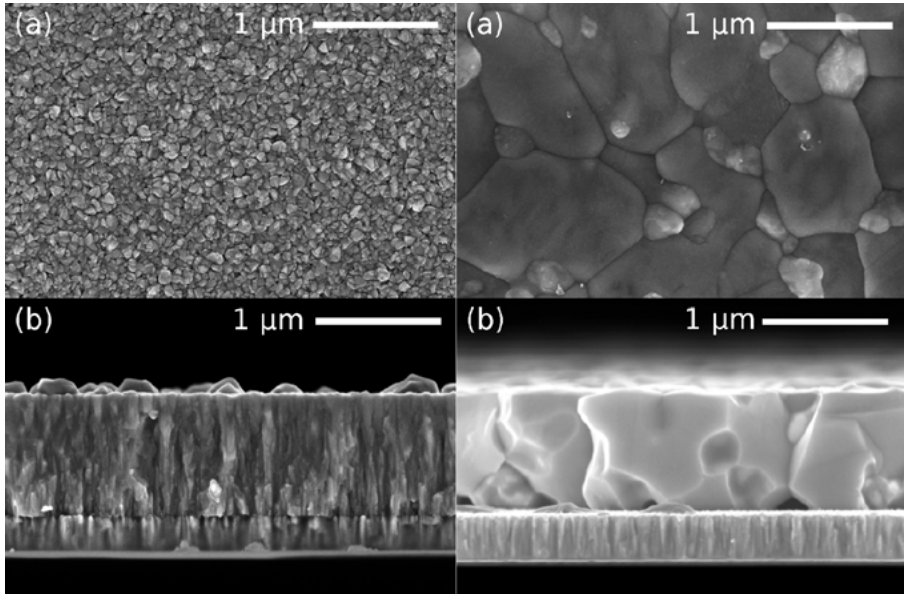


Figure 7. Cross-section scanning electron micrograph of a standard CZTS absorber layer on Mo substrate, before (left hand side) and after annealing (right hand side). (a) depicts top view, and (b) the cross-section view. From [70].

4. Device characterization

In this thesis, the characterization techniques that focus mainly on the device behavior have been employed. These techniques include current-voltage (J-V) and quantum efficiency (QE) measurements, which can be considered the staple of PV device characterization since these techniques give immediate information about the solar cell performance. In-depth analyses with admittance spectroscopy (AS) and capacitance-voltage (C-V) have also been performed. In addition, J-V, AS and C-V are coupled with temperature variation for in-depth analyses.

4.1 Standard test conditions

Standard test conditions (STC) for PV are used as common ground to be able to compare devices made in research as well as commercial PV panels. It means that the efficiency from a measurement is given at $T = 25\text{ }^{\circ}\text{C}$, pressure 1 atm., and an AM.1.5G irradiance spectrum which totals a power density of 1 kW m^{-2} . AM stands for air mass, 1.5 a chosen quantity of the amount of atmosphere the solar irradiation passes before reaching the surface of the Earth, and G for global meaning that both direct light from the sun and diffuse light scattered in the atmosphere is taken into account. Parasitic absorption and scattering due to particles in the atmosphere cause the spectrum to vary with path length through the atmosphere. If a new world record efficiency is to be officially recognized within a certain technology, it needs to be certified at institutes that are recognized as certification bodies, e.g. Fraunhofer Institute for Solar Energy Systems. Commercial PV modules are usually bought with a guarantee to meet several ISO (International Organization for Standardization) and IEC (International Electrotechnical Commission) standards, and test conditions for such standards is a research topic by itself.

Some thin film devices are metastable in nature, as a side-effect from non-stoichiometric compositions and the presence of defect complexes [71, 72], or possibly alternative trace elements, e.g. alkali metals [73], or via a

photo-conductive buffer layer.⁷ In general, there are some states that are the most thermodynamically favorable (global minimum), but require some time to relax into, due to a small energy barrier. Light soaking may change the state of a sample, bringing it to some local minimum. Commonly, the metastable samples show minor transient behavior when exposed to light after some time in dark storage. Under operational conditions with full light bias, these samples are usually stable, but will eventually relax back if stored in dark conditions.

In practice, the metastable behavior means that one carefully has to define the condition in which the characterization is done for it to be comparable. One such procedure is to put the sample in darkness and heat it mildly for an extended period of time to facilitate faster relaxation. A common in-house relaxation treatment is heat treatment at 340 K for 1 h in darkness, similar to relaxation presented elsewhere [74]. This is a good treatment for subsequent analysis in dark conditions since it allows for a point of reference. For characterization done in light biased conditions it may be better to introduce a light-soaking treatment as reference point, e.g. five minute illumination with 1 kW m^{-2} white light.

4.2 Current-voltage

Current-voltage, usually abbreviated J-V for current density vs. voltage, is arguably the most important characterization technique for solar cells. It was utilized in paper I-VII, albeit to minor extent in paper VII. Not only is the power conversion efficiency (η) is given by J-V characterization, it allows for fast measurements that may yield in-depth information on the properties of the solar cells. Two solar simulator J-V set-ups were used in this thesis, a home-built set-up with Quartz Halogen light source with a cold mirror, and a Newport Sol2A system with a Xenon arc lamp. Each set-up is connected to a Keithley 2401 sourcemeter, and utilizes water-cooled sample stages with Peltier elements to maintain a sample temperature of 25 °C.

The characteristic parameters given by a normal J-V measurement are; the short-circuit current (J_{SC}), the current a solar cell produces with no external load in the circuit; the open-circuit voltage (V_{OC}), the maximum voltage that the solar cell will produce with no current flowing in the circuit (open-circuit), and; the fill-factor (FF), an empirical and characteristic parameter that is commonly used to compare devices. FF is a geometrical factor related to η by

⁷ Already in 1948, the conductivity of CdS under influence of illumination was reported by H. Kallman and R. Warminsky, which can affect device performance. Alternative n-type buffer layers, such as Zn(Mg,O) or ZnSnO, can that manifest in a similar manner.

$$FF \equiv \frac{V_{mp} \times J_{mp}}{V_{OC} \times J_{SC}} \quad (17)$$

where $V_{mp} \times J_{mp} = P_{max}$ is the point of maximum power and

$$\eta = \frac{P_{max}}{P_{in}}. \quad (18)$$

For an overview of a light J-V plot, and the characteristic parameters, see figure 8. Additional parameters implicitly given from J-V measurements are discussed in the next section.

In (18), P_{in} is the incoming irradiance, e.g. the standard solar irradiance under AM1.5G conditions. In order to ensure that the solar simulator lamp irradiance is similar to the real solar irradiance, a certified device is used to calibrate the set-up before sample measurements can commence. Due to mismatch in the solar simulator spectrum and the real solar spectrum, if the spectral response of the calibration device is different from that of the samples, e.g. with different bandgap energy, the measurement will be erroneous. In such case it is better to calibrate with a J_{SC} from QE measurement on the sample of interest.

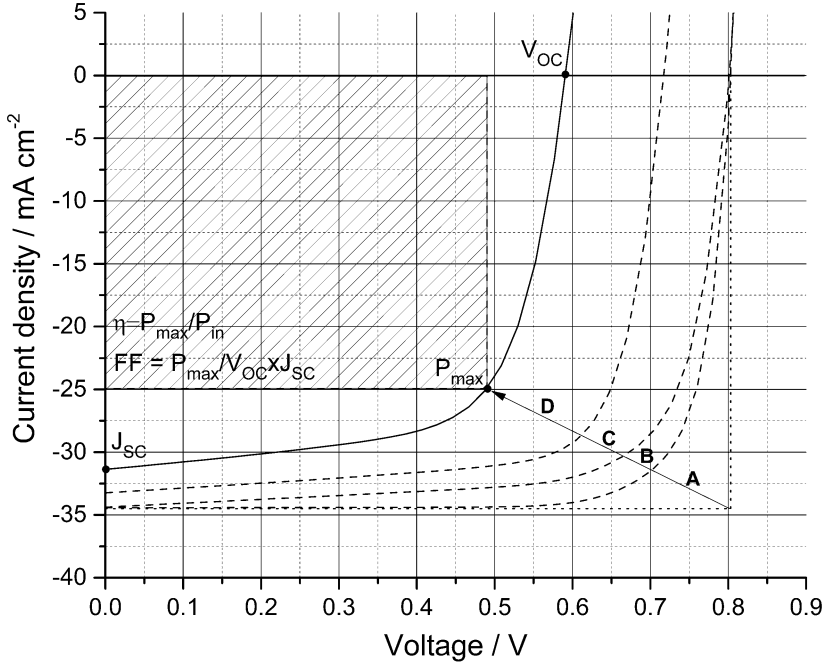


Figure 8. Illustration of J-V curves with; (A), nominal diode behavior; B, Shunt and series resistive losses, lowering the FF; (C), interface recombination that mainly limits the V_{OC} , and; (D), absorber bulk recombination that reduces all J-V parameters and may cause a voltage dependent current collection.

4.2.1 Diode model

In chapter 2 the heart of the solar cell was described; the p-n junction. P-n junctions are more commonly known as diodes and the current flow can be described with [22, 24];

$$J = J_{01} \left[\exp \left(\frac{qV}{k_B T} \right) - 1 \right] + J_{02} \left[\exp \left(\frac{qV}{2k_B T} \right) - 1 \right]. \quad (19)$$

Diodes are known to promote the current in one direction and block the current in the other direction, reflected by the equation above. For positive values of V , referred to as the forward direction from here on out, the current flow in a diode will grow exponentially over two distinct regimes. The first term on the right-hand side of (19) describes the diffusion regime, where

$$J_{01} = \frac{qD_p n_i^2}{L_p N_D} + \frac{qD_n n_i^2}{L_n N_A}, \quad (20)$$

and the second term on the right-hand side describes the recombination regime, which depends on the field at the point of maximum recombination ξ_0 ;

$$J_{02} = \sqrt{\frac{\pi}{2}} \frac{k_B T n_i}{\tau \xi_0}. \quad (21)$$

At low forward voltage bias, the built-in potential in the diode is too high for diffusion current to flow, and the current transport will be determined by recombination in the SCR, reflected mathematically by $J_{02} \gg J_{01}$. Due to the larger exponent in the diffusion term, after some threshold voltage bias, the diffusion term will start dominating at larger forward voltage bias. Figure 9 illustrates the operation of a diode over different regimes. At sufficiently high forward voltage bias the current will be limited by either a high injection regime, when the minority carriers reach concentrations of the majority carriers, or by series resistance somewhere in the circuit, which is not described by (19). In the reverse direction, the current density will saturate at $-(J_{01} + J_{02})$. At further negative voltage bias the diode will eventually go into breakdown. Both the breakdown and the high injection regime are beyond the scope of this thesis.

Noteworthy is that the diffusion term in (19) is called the Shockley equation [75], or ideal diode law, and it is commonly dominating most of the forward voltage bias regime, meaning that the recombination term is often neglected. However, knowing that thin film PV devices are far from ideal it is beneficial to rewrite (19) onto an empirical form, the so called one-diode model:

$$J = J_0 \left[\exp \left(\frac{qV - R_s J}{n k_B T} \right) - 1 \right] + G_{sh}(V - R_s J) - J_L, \quad (22)$$

introducing; J_0 , the saturation current density; n , the ideality factor, also known as the diode quality factor; R_s , the series resistance, and; G_{sh} , the shunt conductance. Both J_0 and n will vary with voltage depending on what regime that dominates, and ideally $J_{01} \leq J_0 \leq J_{02}$, and $1 \leq n \leq 2$, from (19). Depending on the sample characterized with J-V, and what voltage regime is of interest, the empirical parameters may or may not have an influence on the analysis; e.g. R_s will not have an influence on V_{OC} , or the J-V data in general when the current is small. For a diode perturbed by a light source, the light current density J_L describes the current of minority carriers, thus having a negative sign in (22). Since the collection of minority carriers is determined by the quality of the junction, $J_L = J_L(V)$. If the minority carrier diffusion length, according to (15), is large, the voltage dependence is weak. Otherwise the carrier collection is strongly dependent on the SCR width, $W_D \propto V^{1/2}$.

As a final comment on (19) and (22), the -1 ensures that the current is zero (in dark conditions) at zero voltage, but for $V \gg k_B T/q$ it can be neglected. In either case, solving (22) has to be done numerically unless additional approximations are made.

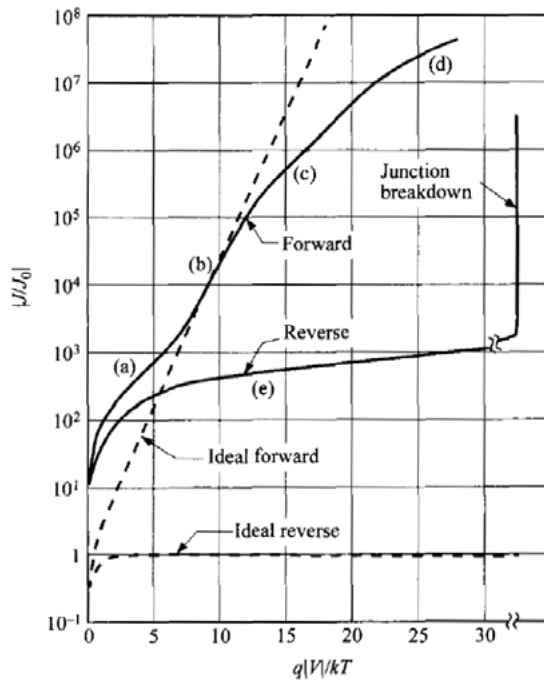


Figure 9. Logarithmic J-V curves showing ideal (Shockley diode) behavior, breakdown and non-ideal diode behavior. (a) represent the recombination regime, (b) the diffusion regime, (c) the high injection regime, (d) the resistive regime and (e) the reverse regime. For thin film devices, the resistive regime may start before high injection regime, thus dominating the J-V curve such that high injection is not visible within the measurement range. Reprint with permission from John Wiley and Sons [22].

4.2.2 Parameter extraction

To extract the parameters in (22) a method was developed by Sites and Mauk [76], and further by Hegedus and Shafarman [77], providing an excellent strategy that will be shortly summarized and discussed here.

First, G_{sh} can usually best be extracted from the dark J-V measurement around zero voltage bias, when $J_L = 0$ and the total current J is vanishingly small reducing (22) to $J \propto G_{sh}V$, such that

$$\left. \frac{dJ}{dV} \right|_{V=0} = G_{sh}. \quad (23)$$

The reasons not to use the light J-V measurement is that (23) will be noisy, due to size discrepancy between $G_{sh}V$ and J_L , and limitation in sensitivity ranges of the sourcemeter. Moreover, voltage dependent current collection may also distort G_{sh} in light-biased conditions.

Second, by defining a resistance

$$r(J) \equiv \frac{dV}{dJ} \quad (24)$$

and plotting $r(J)$ vs. $(J - G_{sh}V + J_{SC})^{-1}$ in the large forward bias regime it is possible make a linear fit which will intersect with the y-axis. The intersection is an estimate of R_s and the slope is proportional to $nk_B T/q$, thus yielding the ideality factor. This plot will generally be scattered, or cover large range of values due to both the reciprocal and the derivative, but it is only the last voltage points that are of interest, closest to origin, as seen in figure 10.

Finally, plotting $\log_{10}(J - G_{sh}V + J_{SC})$ vs. $V - R_s J$ should give a linear curve over a couple of decades. By making a linear fit over the relevant region the slope will be proportional to $q/nk_B T$, once again making it possible to extract the ideality factor. In addition, the intersect with the y-axis will give J_0 .

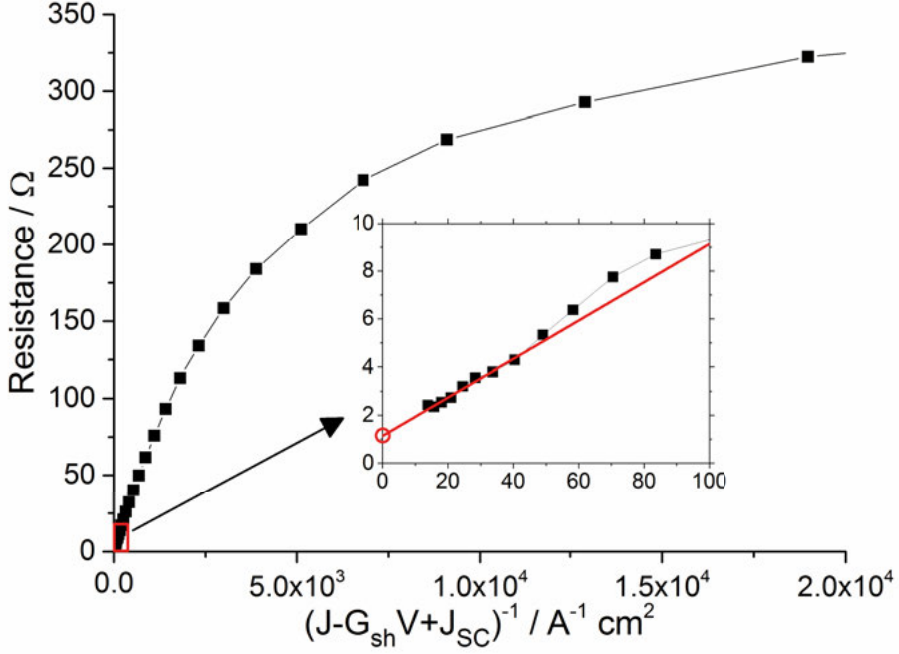


Figure 10. The resistance calculated in (24) plotted against the reciprocal of the normalized current. Only the last voltage points are of interest to extract an accurate R_s .

4.2.3 Temperature variation

There is additional information to extract from J-V characterization when a temperature variation is added (J-V-T), most importantly the dominant recombination path. The saturation current J_0 can be written on the general form [22, 44]

$$J_0 = J_{00} \exp\left(\frac{-E_A}{nk_B T}\right) \quad (25)$$

where $J_{00} \propto T^\gamma$ is considered weakly temperature dependent relative the exponential behavior, and E_A is the activation energy of the dominant recombination path. If the bulk of the absorber is the limiting factor, then $E_A = E_g$, from (9) and (20), illustrated in figure 5 by (A-C). On the other hand, if the recombination at the interface is dominating, then $E_A \leq E_g$. Depending on the carrier concentrations, and charge around and at the interface, commonly $E_A = \Phi_b^p$ where $\Phi_b^p = E_{Fn} - E_V$ if the quasi Fermi level of the electrons is pinned, otherwise $\Phi_b^p = E_C - E_V$, and E_V is the highest valence band edge energy on either side of the junction, and E_C is the lowest conduction band edge [44]. To differentiate between recombination in the quasi neutral bulk and in the SCR one may look into the ideality factor. In most

cases, a multitude of recombination pathways are active, including the back contact surface, and E_A is seldom matching one specific activation energy, and n seldom is exactly 1 or 2.

With J_0 and n known, one can construct an Arrhenius diagram plotting $n \ln J_0$ on the y-axis. Thus, the energy can be extracted from the slope of a linear fit. In this way, also the temperature independent pre-factor J_{00} can be extracted from an extrapolation to the y-axis. However, extracting J_{00} is coupled with uncertainty of J_0 in conjunction with high sensitivity of extrapolating to the logarithmic y-axis. In paper II, a variant of this procedure was tested, taking into account a temperature dependent activation energy, based on a method developed by Hages et al. [78].

Another way to extract the activation energy is to combine (22), (25) and $V_{OC} \gg k_B T/q$, for a point $J(V = V_{OC}) = 0$, assuming that G_{sh} is negligible;

$$J_L = J_{00} \exp\left(\frac{-E_A - qV_{OC}}{nk_B T}\right). \quad (26)$$

By re-arranging (26) into

$$V_{OC} = \frac{E_A}{q} + \frac{nk_B T}{q} \ln\left(\frac{J_L}{J_{00}}\right) \quad (27)$$

it is evident that a plot of V_{OC} vs. T should exhibit a linear regime. A linear extrapolation of this regime to $T = 0$ K will yield the activation energy. There is one caveat with this method, it is assumed that no other parameter exhibits a temperature dependence. It is, however, easy to check n for which $n(T)$ is constant, and use these points for the linear fit, something that was the preferred method in paper II and III. One should make sure that J-V is measured at sufficiently narrow-spaced temperature points in order to make statistically good linear fit of $V_{OC}(T)$. See figure 18 in chapter 6, for an example of this method used to extract the activation energy, as well as an example of an unsuitable set of data with a temperature dependent ideality factor.

In general, since temperature dependent measurements are time consuming, it is always good to plan the measurement accordingly; taking more measurement points where one expects something interesting to be revealed, and possibly fewer steps in other regions. In-house J-V-T is done in the same homebuilt set-up where AS and C-V is measured; a liquid N_2 cooled cryostat and a LakeShore 325 temperature controller unit. The light bias comes from a set of red, green, blue and white diodes that can be controlled individually.

4.3 Quantum efficiency

Second to J-V, QE is the most common characterization technique used for solar cells. In short; QE is the ratio between number of electrons in the output current and the incoming photons with a given energy. In the set-up, a Xenon arc lamp is used together with a monochromatic filter wheel. By varying the light beam from UV to IR at known intensities, and simultaneously measuring the output current density J_{out} , here in units of $\text{mA cm}^{-2} \text{ nm}^{-1}$, the QE can be measured;

$$QE(\lambda) = \frac{J_{out}(\lambda)}{q\Phi_{in}(\lambda)}, \quad (28)$$

where $\Phi_{in}(\lambda)$ is the known incoming photon flux of the measurement light beam. The output current can be normalized to any spectrum, e.g. the AM1.5G. Since $J_{SC} = \int J_{out}(\lambda)d\lambda$ we get

$$J_{SC} = q \int QE(\lambda)\Phi_{AM1.5G}(\lambda) d\lambda. \quad (29)$$

It means that a good estimate of the real (AM1.5G standard) short-circuit current can be given with a QE measurement, and detailed analysis of the QE curve will yield further information.

One caveat of QE is that the monochromatic light beam is of low intensity. While noise from the background is effectively removed by chopping the light signal and using a lock-in amplifier, this in itself is not a problem. However, due to the complex nature of thin films and their response to full light illumination, the characteristics from the QE measurement may be somewhat different for a measurement in dark conditions, or weak ambient light, as compared to having a full 1 kW m^{-2} light bias.

4.3.1 Internal quantum efficiency

Two types of losses are discernable from the QE measurement, optical losses and collection losses. The optical losses are due to reflection, parasitic absorption, generation losses and possibly shading, while collection losses are due to absorber bulk and surface recombination. The different losses are illustrated in figure 11. Since reflection of a stack can be measured, it is possible with such a measurement to construct the internal QE (IQE) from the external QE (EQE):

$$IQE(\lambda) = \frac{EQE(\lambda)}{1-R(\lambda)}. \quad (30)$$

Thus, the other losses are easier to evaluate, and the possible gain of an anti-reflective coating can be better estimated. If the absorption coefficients of

each layer in the device stack are known, it is possible to evaluate the collection efficiency, e.g. with device modeling.

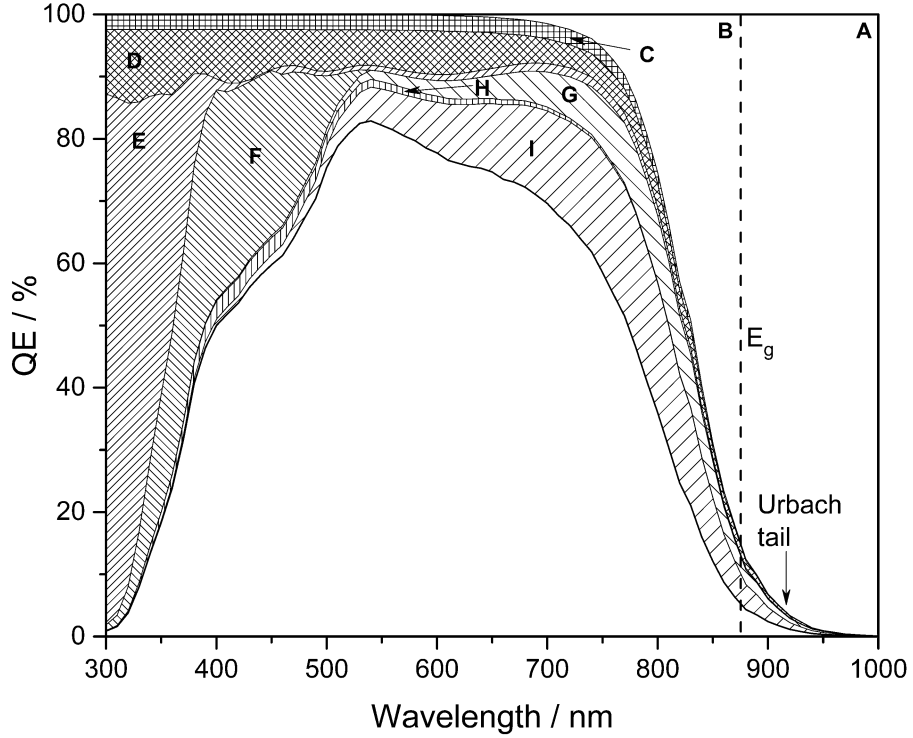


Figure 11. An illustration of the losses seen in a QE measurement. (A) is sub-bandgap generation losses, (B) incomplete absorption, (C) shading from the metal grid, for a module, this would correspond to the dead area between cells, (D) front surface reflection, (E) parasitic absorption in i-ZnO and the TCO, including free carrier absorption at longer wavelengths, (F) parasitic absorption in CdS buffer layer, (G) back contact recombination, (H) interface recombination, and (I) bulk recombination. The Urbach tail consists of exponentially decreasing tail states from valence and conduction band edges, due to imperfections in the crystal lattice.

4.3.2 Voltage dependent quantum efficiency

Voltage dependent QE (QE-V) are primarily done over a range of reverse voltage biases in order to evaluate the magnitude of the voltage dependent carrier collection. The discrepancy between the slope of dark and light J-V around 0 V should in principle correlate with the magnitude of the current gain with reverse voltage biased QE. Knowing the width of the SCR, simulating QE-V can be used to estimate the diffusion length. One can also apply semi-empirical models, combining QE-V and C-V, to analytically extract the absorption coefficient and diffusion length with [79]:

$$IQE(\lambda, V) \approx 1 - \frac{\exp[-\alpha(\lambda)W_D(V)]}{\alpha(\lambda)L_n + 1}. \quad (31)$$

4.3.3 Bandgap extraction

There are different ways to extract the bandgap from a QE measurement, each with its own set of approximations and therefore systematic and random errors embedded. Hence, whenever a bandgap is extracted from QE, it is important to state with what model it is extracted. Employing the same model and method consistently is usually more important than the exact quantity of the bandgaps, so that the values are comparable.

The most commonly used in-house method is based on (31). Close to the bandgap $\alpha(\lambda)$ should drop rapidly, and with a limited diffusion length (31) can be rewritten

$$IQE(\lambda) \approx 1 - \exp[-\alpha(\lambda)W_D] \quad (32)$$

and going one step further with an expansion around $\alpha(\lambda) = 0$

$$QE(\lambda) \propto \alpha(\lambda). \quad (33)$$

The probability of light absorption is proportional to the available number of states for the electrons to inhabit, i.e. the density of states (DOS), and in 3D: $DOS \propto \sqrt{E}$. Thus,

$$QE(\lambda) \propto \sqrt{\frac{hc}{\lambda} - E_g} \quad (34)$$

around the bandgap energy, which means that a plot of $QE(E)^2$ vs. E will yield a straight line for energies slightly above the bandgap energy. The final step is to fit a straight line and extrapolate to the x-axis. This method is easy to use and gives a good estimate of the bandgap, but it does involve both approximations, as described, and an element of human error due to the fitting.

A second method, used in literature [56], is to simply extract the value of the inflection point of the regime where QE drops. This empirical method is straightforward and consistent, but challenging when the QE data is noisy, and moreover, does not have a physical meaning. Thus, the bandgap value will rather be a “near-bandgap-value”. A third and fourth method to extract E_g with QE includes plotting $(QE \times E)^2$ or $[E \ln(1 - QE)]^2$ vs. E . In an internal study by S.-Y. Li [80] it was found that each of the QE-derived methods are sensitive to absorber thickness. In the study, method one and three was seen to underestimate E_g , for regular thin film thicknesses, while method two and four were more robust to thickness variation. Due to the flaws of method two mentioned above, plotting or $[E \ln(1 - QE)]^2$ vs. E may be the best choice to extract the bandgap value.

4.4 Admittance spectroscopy

AS is a characterization technique where a small signal current \tilde{J} is measured as a function of a voltage \tilde{u}_{ext} modulated with frequency ω :

$$Y(\omega) = Z^{-1}(\omega) = \frac{\tilde{J}}{\tilde{u}_{ext}}, \quad (35)$$

where Y is the complex admittance and Z is the complex impedance. The in-house set-up is home built with Agilent 4284 precision LCR meter and temperature controlled sample stage with four point probes. The system is capable of frequencies 100 Hz to 1 MHz. Of main interest in this thesis is the capacitive behavior, and thus an equivalent circuit model has to be applied to the measured data before the capacitance can be extracted. For p-n junctions in solar cells it has been shown that a parallel circuit with a resistance (R_p) and capacitance (C_p) [81] is usually appropriate. Thus, the imaginary part of the admittance within the parallel circuit representation;

$$Y = G_p + j\omega C_p \quad (36)$$

is used to extract the capacitance. For simplicity, onward the index p will be omitted from C , and no differentiation will be made between capacitance or capacitance per unit area. In the ideal case the plate capacitance relation can be used,

$$C = \frac{\epsilon_r \epsilon_0}{d}, \quad (37)$$

where ϵ_r is the relative permittivity of the dielectric, ϵ_0 the vacuum permittivity and d the thickness of the dielectric. In the case of a p-n junction, $d = W_D$ (the SCR width). In practice, other dielectric layers present in the structure may contribute to the capacitance. Assuming a sandwich structure, with layers on layers that constitute only a 1-D variation, where the electric probes goes in either end of the structure, one can approximate all individual capacitances in the structure to be in series with each other. In such case, one should consider that the total capacitance may be dominated by the smallest capacitance:

$$C^{-1} = C_1^{-1} + C_2^{-1} + \dots \quad (38)$$

In the presence of deep defects, see figure 12, there is a contribution to the junction capacitance if the defects are fast enough to react to the frequency of the ac-modulation, and if the trapping and de-trapping of the defects is plausible, i.e. if the Fermi level crosses the defect energy level. The detailed theory for this in regards to thin film solar cells is outlaid by Walter et al.

[82], and similarly in non-equilibrium by Decock et al. [83]. In short, the energy required to change the charge state of a defect is in static conditions dependent on the Fermi level in relation to the defect energy level and the capture cross-section of the defect. For ac-modulation, however, the probability of a change in charge state will depend on the frequency. For a p-type material, and where charge response is limited by hole emission from the defect in question:

$$E_\omega = k_B T \ln \left(\frac{N_V v_{th} \sigma_p}{\omega} \right). \quad (39)$$

Whenever a deep defect cannot follow the ac-modulation, a relaxation occurs. For frequencies above the characteristic frequency, $\omega_0 = \omega$ in (39), the defect no longer contributes to the junction capacitance. This frequency dependent activation energy is sometimes referred to as the demarcation energy. However, one should be aware that a drop or step in capacitance might come from a circuit response if there is a non-negligible series resistance present. One can calculate the onset of the drop from the cut-off frequency

$$f_0 = \frac{1}{2\pi R_s C_p}. \quad (40)$$

The primary use of AS in this thesis is to choose an appropriate frequency for capacitance-voltage measurements, but it is also used for more advanced characterization, e.g. when adding temperature variation.

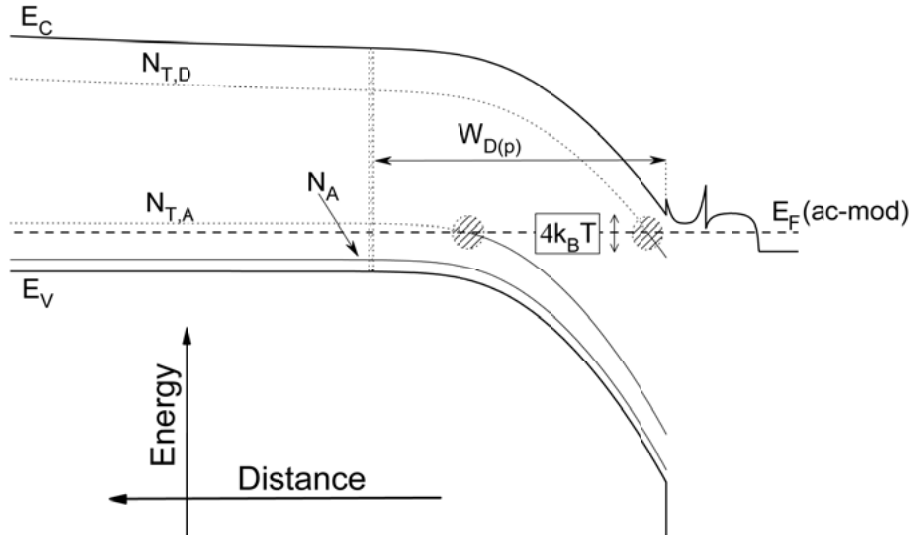


Figure 12. An illustration of the absorber band diagram at 0 V AS. with the contributions to capacitance from deep defects [82] given by the “striped” areas at the edge of the depletion region and where the Fermi level crosses the defect energy levels.

4.4.1 Temperature variation

Adding a temperature variation to AS enables the extraction of deep defect activation energy per (39). The term in the logarithm $N_V v_{th} \sigma_p \propto T^2$, and thus; an Arrhenius diagram of $\ln(T^2/\omega)$ vs. $1/k_B T$ will yield E_ω on the slope of a linear fit.

4.5 Capacitance-voltage

In the same theoretical framework, and with the same equipment, as admittance spectroscopy, the parallel capacitance can be extracted as a function of dc voltage bias to constitute a C-V measurement [22, 84]. A small ac-modulation with a set frequency is superimposed on the dc bias. The amplitude of the ac-modulation is of the order 10 mV, and the dc voltage bias interval is chosen appropriately for the sample. Reverse voltage is usually limited by diode breakdown, and forward voltage bias is limited by the injection of charge carriers from the buffer into the absorber. In the results, chapter 6, a typical C-V plot is shown. Knowing that the measured capacitance follows (38), it becomes evident that with a larger SCR in the absorber, the smaller the depletion capacitance, and thus larger part of the total capacitance. This happens at reverse dc voltage bias. At more positive dc bias the SCR shrinks and contribute less to the capacitance, at which point the total capacitance will be determined to larger extent by some other, lower, capacitance in the structure.

4.5.1 Measurement frequency

The frequency set for the C-V measurement should depend on the sample and the motivation behind the experiment. Most commonly the doping concentration is of interest, and in such a case one should choose the highest possible frequency, preferably above the characteristic frequency of any deep defect present in the material, but where a good signal is still achievable. A good signal means that a substantial part of the admittance signal is capacitive, i.e. that a high negative phase angle is obtained. Moreover, it is good practice to choose a frequency where the AS shows little or no frequency dependence, i.e. on a plateau, meaning that variations in the sample or in measurement conditions do not result in a significant change of the capacitance. For CIGS and CZTS there are a couple of caveats: Knowing that deep defects will contribute to the junction capacitance, as stated, it is preferable to measure at a higher frequency where they do not respond. However, at room temperature this regime can occur at frequencies higher than the measurement range. To characterize the regime after the capacitance step, one may need to decrease the temperature, but at lower temperatures the capacitance usually goes toward majority carrier freeze-out and a geo-

metrical capacitance; the capacitance for the whole absorber layer. In other words, the main acceptor in the absorber is not ionized and does not contribute to doping, and the absorber layer behaves like a dielectric. For CZTS, there seems to be no middle ground. Part of the reason may be the fact that the defect with lowest formation energy in CZTS is the Cu_{Zn} acceptor [66, 85], with a higher energy level above the valence band as compared to V_{Cu} . In CIGS, V_{Cu} is the dominant acceptor since it has the lowest formation energy in that system, and is the most shallow acceptor in both CZTS and CIGS [45, 66].

4.5.2 Doping concentration

In theory, the depletion capacitance for an abrupt one-sided p-n⁺ junction is [22]

$$C_D = \frac{\epsilon_r \epsilon_0}{W_D} = \sqrt{\frac{q \epsilon_r \epsilon_0 N_A}{2}} \left(V_{bi} - V - \frac{2k_B T}{q} \right)^{-1/2}. \quad (41)$$

Rearrangement of (41) gives us the basis for the so called Mott-Schottky plot, namely

$$\frac{1}{C_D^2} = \frac{2}{q \epsilon_r \epsilon_0 N_A} \left(V_{bi} - V - \frac{2k_B T}{q} \right), \quad (42)$$

which is used to evaluate the doping and built in potential by plotting $1/C_D^2$ vs. V , where the slope is inversely proportional to N_A , and an extrapolation to the x-axis will give $V_{bi} - 2k_B T/q$. The beauty of the Mott-Schottky plot is that it, comparatively, gives you an idea of the doping concentration from a C-V measurement. Unless quantitative values are wanted, no additional approximation or fitting is required. If quantification is wanted, then a doping profile can be constructed where

$$N_A(W_D) = -\frac{2}{q \epsilon_r \epsilon_0} \left[\frac{d(1/C_D^2)}{dV} \right]^{-1}. \quad (43)$$

As emphasized in (43), the doping concentration is given at the edge of the depletion region which, naturally, is moving with dc voltage bias. If a sample is uniformly doped, then the Mott-Schottky plot will yield a straight line and the doping profile will be constant. For thin film solar cells, this is rarely the case; not only are there possible deviations from uniformity when it comes to the shallow doping, but there might also be a contribution from deep defects to the capacitance at sufficient reverse bias conditions. An example of non-uniform doping is given in paper I where a defect model incorporating an ambivalent defect complex which changes from a single donor to a double-acceptor defect close to the interface to the buffer layer [71].

In fact, the ambiguity of knowing what contributes to doping, and what is deep defect contribution to junction capacitance, and how this affects the analysis, leads us to name N_A in (43) the *apparent* doping concentration. In C-V analyses it is very common to plot the doping profile, N_A vs. W_D . For thin film solar cells, a U-type doping profile is usually seen, where the framework of Kimerlin [86] is widely used to justify the extraction of shallow doping concentration. N_A is then taken to be the lower most value in the doping profile, and at larger W_D the increase is attributed to deep defects. For smaller W_D the analysis is usually uncertain due to injection of electrons from the n-side. Paper VII is focused on simplifying the experimental sample structure and get a better estimate of N_A , and quantify the difference obtained from the different structures. See chapter 6 for C-V and Mott-Schottky plots.

5. Device modeling and simulations

As stated in the introduction, modeling forms a bridge between theory and experiment. This chapter is dedicated to the main modeling tool that has been used throughout this thesis, the Solar Cell Capacitance Simulator (SCAPS) [19], including discussions on some common pitfalls and how to avoid them.

5.1 SCAPS-1D

SCAPS is a free software and was introduced in 1996 [87], and since then it has undergone improvements and added functionality [88-93]. It is specifically created to be able to model thin film PV systems, and a good description of what is required to handle that is given in [19]⁸.

SCAPS is programmed to solve the basic semiconductor equations, given in chapter 2, and to handle up to seven layers of different materials, in addition their interfaces. Each layer has physical properties that can be made to vary as functions of the layer thickness, or vary with a compositional variation. This makes SCAPS very versatile. However, it is not uncommon that SCAPS fails to make a solution converge if some physical parameter lies beyond what is commonly observed for thin films. In fact, it may even allow parameters to be set independent of each other, even though there should be a relation between them, putting a larger requirement on the user.

A big strength of the program is that one can monitor much more than just the characteristic parameters. An example of this is that one can easily plot the recombination profile in the model, i.e. $U(x)$ and cumulative recombination, starting at either contact, $\sum U(x)$. This particular example is mentioned since $U(x)$ will give you the total *bulk* recombination profile, while $\sum U(x)$ includes surface and interface recombination. Thus, $\sum U(x)$ is the better option if back contact surface or absorber/buffer layer interface recombination is of interest. Another important note is that if a comparative study is made, and some parameters are investigated e.g. around V_{OC} , the

⁸ So far, the only requirement from the user to get and run the program has been to contact the creators, prof. Marc Burgelman et al, previously at Ghent University. Prof. Burgelman has been retired since 2016 and it is currently unknown whether further improvements to SCAPS will be added. The latest version of SCAPS available for public use is currently version 3.3.02.

actual working point for the results may vary slightly depending on the voltage step size. Due to the exponential J-V behavior, this may lead to a misinterpretation of the data, e.g. that interface recombination is more detrimental in one case compared to another, just because the relative working point is different in the comparison.

5.1.1 Input parameters

Input parameters that are fundamental for device modeling are the ones required to solve the basic equations and the related theory mentioned in chapter 2. In table 1, a summary of the bulk and interface parameters are given. In each of the seven layers, one may specify a thickness variation $y(x)$, e.g. model a compositional variation. This is done by specifying the extreme values and the interpolation function. In table 1, these parameters are marked being functions of x . There is also an option to vary some of the parameters with the composition, marked in the table with functions of y . Between each layer one can define an interface with defects, either to carry charge, act as recombination centers, or both, much like bulk defects N_T .

SCAPS handles optics in a simple manner; it calculates absorption of light according to Beer-Lambert attenuation, see (45) in chapter 6. Since no complex optical constants are handled, no interference is calculated either. Wavelength dependent reflection and transmission (R-T) can be added as an optical filter at the front and back contact. In addition, SCAPS being a 1-D modeling tool means that scattering and roughness cannot be included explicitly.

All parameters are to some extent important in SCAPS, but the influence of each parameter will depend on the model. For a low performing device where SRH recombination, see (12), is the dominant limiting factor of the absorber material, radiative recombination might be negligible. In a high efficiency model, neglecting radiative recombination might give large errors in the J-V simulations. In addition to input parameters, it is also possible to specify the voltage working point, temperature and illumination.

5.1.2 Creating a model

Some of the work in paper I, II, IV and VII are based on modeling done by J. Pettersson [94]. There are two common objectives for creating a device model: 1) To verify and understand the behavior of real devices and, 2) to simulate the behavior for given parameter variations, thus; predicting the outcome for those parameter changes in reality. A good model is defined by how well simulations reflect the behavior of the reference device(s) it was made for from the start. One can also choose whether to model an average behavior of many samples, or the behavior particular to a device that represents the reference. As with any type of fitting, the more free (unknown) parameters in the model, the easier to do the fitting. This means that in creat-

ing a model, top priority should be given to fix as many parameters as possible, preferably from experimental data collected from the reference device(s). Otherwise, literature values can be used.

In table 1, the parameters are divided (dashed lines) into segments representing how they were commonly chosen in this thesis. The first segment belongs to parameters extractable from experimental data, profilometry, X-ray fluorescence, PL, ellipsometry, R-T, J-V and C-V. The second segment contains parameters that were gathered from literature, either experimental or theoretical, and the last segment are the commonly used fitting parameters.

Table 1. The most important modelling parameters in SCAPS, in order of input priority as described in section 5.1.2.

Parameter	Property	Unit	Comment
d	Layer thickness	μm	x-direction
$y(x)$	Composition	<i>a.u.</i>	Function or vector
$E_g(y)$	Bandgap energy	eV	$E_C - E_V$
$\alpha(\lambda, y)$	Absorption coefficient	cm^{-1}	Decides generation
$R(\lambda)$	Reflection, back and front	%	Front = stack reflection
$R_{s,sh}$	Series/shunt resistance	$\Omega \text{ cm}^2$	Given externally
$N(x, y)$	Doping concentration	cm^{-3}	p- or n-type
$\epsilon_r(y)$	Dielectric constant	$\epsilon_o (\text{F m}^{-1})$	Relative permittivity
$\chi(y)$	Electron affinity	eV	$E_{\text{vacuum}} - E_C$
$\mu(y)$	Mobility	$\text{cm}^2 \text{ V}^{-1} \text{ s}^{-1}$	Important for collection
$m^*(y)$	Effective mass	$m_0 (\text{kg})$	Crystal prop.
v_{th}	Thermal velocity	cm s^{-1}	Rel. effective mass
$N^*(y)$	Effective density of states	cm^{-3}	Order of magnitude
$B(y)$	Radiative rec. coefficient	$\text{cm}^3 \text{ s}^{-1}$	Scales with α
S	Surface rec. velocity	cm s^{-1}	Back and front contact
$N_T(x, y)$	Bulk defect concentration	cm^{-3}	SRH rec. (12)
$E_T(y)$	Defect energy level	eV	SRH rec. (12)
$\sigma(y)$	Capture cross-section	cm^2	SRH rec. (12)
Φ_M	Metal work function	eV	Back and front contact

5.2 Simulations

SCAPS offers single simulations of J-V, QE, C-V and AS, and more advanced batch simulations where any input parameter can be varied. With batch simulations, it is also possible to monitor certain pre-defined physical parameters, such as efficiency or electron concentration, as a function of the varied batch parameter.

Nominally, simulations of both J-V and QE in a device model should resemble the corresponding reference measurements. Following is a short de-

scription on the simulations used in this thesis, and the methodology involved.

5.2.1 Current-voltage

J-V simulations has been a primary tool to evaluate and fit a model to a reference device, used in paper I, II, and somewhat in paper IV. Beyond the characteristic J-V parameters J_{SC} , V_{OC} , FF and even η , a good fit of simulated J-V versus the experimental data should apply to the whole J-V curve. This means that the shape of the J-V curve might be more important than the exact quantity of the characteristic parameters.

Standard in-house devices have a contact grid on top of each cell, covering about 2.5 % of the surface area, meaning that unless corrections are made, the model should simulate a 2.5 % higher J_{SC} compared to measurements. In chapter 4, the conditions of a measurement were described. Since physical properties of CIGS and CZTS samples may vary in light and darkness, this is something to consider if discrepancy between measurement and simulation is found when performing dark and light J-V simulations within a single model.

5.2.2 Quantum efficiency

QE is best simulated in SCAPS if a reflectance filter at the front is used in the model. With optical filters, it is easier to model a correct minority carrier collection, one of the main goals with QE simulations. Using a filter reduces part of the drawback with the way SCAPS handles optics.

QE simulations were used mainly in paper I and II, and coupled with J-V simulations. In contrast to J_{SC} in J-V, it does not need to be corrected for normal QE measurements as long as the spot size of the light fits between the grid fingers on the samples.

5.2.3 Capacitance-voltage

C-V simulations were done mainly for an alternative structure that was investigated in paper VII. SCAPS simulates according to the basic equations presented in chapter 2, but conveniently produces data applying the same approximations that are presented in the AS and C-V section of chapter 4 so that measurements and simulations are easily comparable.

6. Results and discussions

Herein, the key results from the papers included in the thesis are presented, including some additional results and discussion on related topics. In the same order as the papers appear, I first discuss the high-efficiency CIGS model, and then continue with the baseline CZTS model with a discussion on some of the crucial efficiency losses and how to minimize interface recombination. Next, a discussion of doping concentration and how to evaluate it in CZTS is included. Finally, I discuss the potential of efficiency enhancement in CZTS with the inclusion of selenium to modify the bandgap in a similar way to the high efficiency CIGS case. Every model was created following the methods described in chapter 5.

6.2 Ga-profile optimization in CIGS

In paper I, a device model was created based on a high performing CIGS solar cell reference device, with the aim to optimize the Ga-profile, according to (16), for highest possible efficiency. Modeling of Ga-profiles or bandgap gradients prior to our work showed diverse results, from positive [95-97] to more critical [98, 99] conclusions. Decock et al. [90] made a good statement that Ga-profile engineering may be good if generation and recombination can be controlled in such a way that it is beneficial for the device.

The absorber layer of the device was created with co-evaporation using static sources and sample holder, and varying the evaporation rates to simulate an in-line process. The Ga-profile of the device was estimated with glow discharge optical emission spectroscopy (GD-OES) and energy-dispersive X-ray spectroscopy (EDS) of a transmission electron microscopy sample on three different grains. The GD-OES creates a laterally averaged profiles, and the EDS high resolution Ga-profiles in cross-section. From figure 13 it is clear that the composition and thickness varies laterally in the thin film. Each EDS grain 1-3 line in figure 13 represents an average of ten sweeps, and the average of the three lines were used as input to the model.

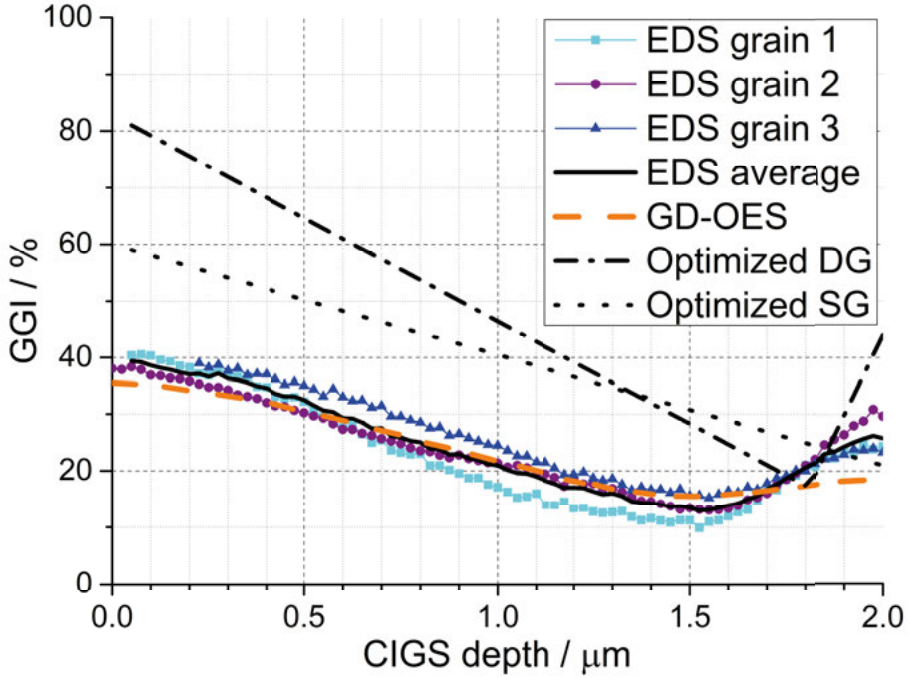


Figure 13. The GGI as a function of absorber thickness, zero on the x-axis indicating the back contact. The optimized Ga-profiles are from model B, and every optimized Ga-profile can be found in paper I. DG = single graded and DG = double graded.

Since it is known that CIGS thin films are inherently defect rich, see chapter 3, four different models were created, named A-D. Model A is a simple defect model with a spatially homogenous distribution of mid-gap recombination centers, following SRH formalism according to (12). Model B takes into consideration that CIGS quality deteriorates after an optimum composition of $\text{GGI} \approx 0.3$ [100], which manifests in a non-linear increase of V_{OC} with increasing E_g , see (27), only in part due to a non-ideal CBO towards the CdS buffer layer, and an overall worse absorber quality. Model C incorporates an inhomogeneous doping profile due to an added amphoteric defect complex that changes from a single donor to a double acceptor (in the bandgap) according to theory [71]. Finally, model D incorporates the defects present in both model B and C. Defects have two major roles to play in the model, their contribution to charge distribution, which affects (4), and their impact on the minority diffusion length (15), by limiting the lifetime (14). The key modeling parameter quantities can be found in table 1 in paper I. Good fits of both J-V and QE were achieved with all models, following the general method outlined in chapter 4, see figure 14.

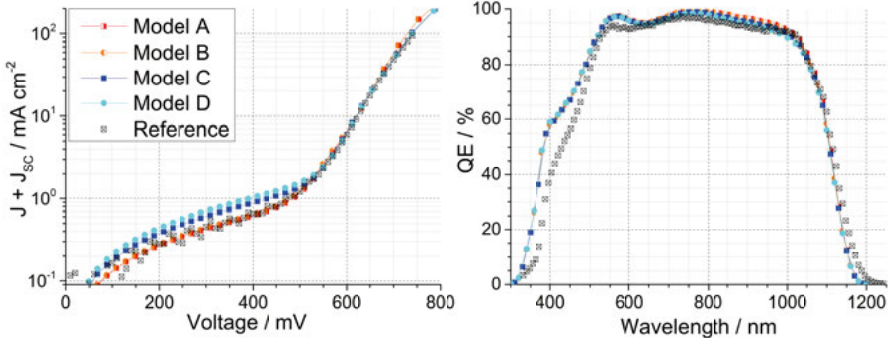


Figure 14. The J-V curve of the models compared to the measured reference device, on the left hand side. The QE from each of the models on the right hand side, including the reference measurement.

GGI was varied both as linear single graded (SG) and double graded (DG) Ga-profile, and the Ga-profiles of model B yielding highest efficiency are presented in figure 13. The common feature for both single and DG profiles is the back grading which functions to enhance the collection with both the quasi-electric field and simultaneously by acting as a back contact barrier. The overall increase in GGI means an overall lowering of generation due to the higher average bandgap, but acting as a trade-off with voltage. The front grading of the DG Ga-profile is beneficial and may yield higher efficiency if interface traps are present, albeit with only a small difference. This manifests as a V_{OC} increase at a small expense of FF , comparing the optimized DG with the optimized SG Ga-profiles. One way to look at it is that generation and charge carriers are moved away from the critical junction. However, for sharp DG Ga-profiles, the notch, i.e. the minimum, can be a bottleneck if not placed within the SCR because of the accumulation of minority carriers. The average GGI = 0.40 for the optimized SG Ga-profile, and average GGI = 0.47 for the optimized DG Ga-profiles, are both substantially higher than average GGI = 0.24 for the reference device. As always, with bandgap variation, there is a trade-off between current and voltage. One might expect that a uniform composition would end up being higher in GGI compared to the reference, taking the detailed balance principle into account. However, the system is far from ideal and there are many physical properties that factor into the end product; surface recombination, band alignment, bulk defects, absorption coefficient, etc. As such, there is no rule of thumb and the optimum Ga-profile, be it uniform or DG, will depend on each of these factors. It also means that the efficiency dependence will have a soft peak, and be tolerant to some variation of GGI.

Table 2. The characteristic J-V parameters, saturation current density and ideality factor according to equation (22).

Model	V_{oc} / mV	J_{sc} / mA cm ⁻²	FF / %	η / %	J_0 / A cm ⁻²	n
Reference	685	36.8	75.9	19.1	1.38×10^{-9}	1.56
A	680	38.1	75.7	19.6	4.5×10^{-10}	1.45
B	681	38.0	75.4	19.5	6.1×10^{-10}	1.47
C	687	37.8	75.6	19.6	3.7×10^{-10}	1.45
D	685	37.6	75.8	19.5	4.5×10^{-10}	1.46
B-SG	746	35.1	79.4	20.8	2.8×10^{-11}	1.39
B-DG	790	35.0	77.4	21.4	0.8×10^{-10}	1.55
B-DG*	790	35.0	77.6	21.5	2.8×10^{-10}	1.65
B-SG	779	35.2	77.7	21.3	4.1×10^{-10}	1.66
B-DG	792	35.0	77.3	21.5	3.0×10^{-10}	1.66

*Indicating a non-restricted optimized Ga-profile, where the notch is within 40 nm of the front interface, see details in paper I.

The top efficiency was predicted to be around 21.5 %, given in model B, see table 2. The overall difference between the modeled optimized Ga-profile, in each respective defect model, was a slightly higher GGI at the notch for model C and D, with higher doping close to the interface due to the amphoteric defects. In addition, the optimum efficiency in these models were approximately 0.5 % (absolute) lower compared to model A and B, for the DG optimized Ga-profiles. In the SG optimization, a negligible difference was seen. In general, the optimized Ga-profiles in the models were consistent in-between each other.

Shortly before publishing paper I, ZSW fabricated several devices with efficiencies above 20 % [101], and the Ga-profiles, although DG, were slightly varying between each other. It is likely that their efficiency improvement was not a product of optimized Ga-profile, but by well-behaved back contact, front interface and an overall good absorber quality: E.g., with a back contact that does not sink electrons, the tolerance will be high for a variation of back grading. Since then, EMPA, Solibro Research AB, Solar Frontier and ZSW have all been close to 22 % or higher. An optimized Ga-profile was not the sole improvement on those cells, compared to previous records; the PDT with heavy alkali metals played the major role. In general, the room for error is quite small for high performance, and since part of the Ga-profile optimization is to construct more favorable recombination profiles, with already good conditions the tolerance for a varying Ga-profile may grow larger.

6.2 Bottlenecks in high efficiency CIGS devices

With efficiencies beyond 20 %, it is observed that SRH recombination no longer dominates total bulk recombination, and radiative recombination becomes increasingly detrimental, in agreement with other studies [102]. It means that CIGS crystal quality may soon be as good as it ideally can, and that there are other bottlenecks that become relatively more important. In figure 15, the bulk recombination profiles for the high efficiency model B is simulated in open-circuit conditions. Surface and interface recombination is not seen, and the drop in bulk recombination towards the back contact surface is due to a small electron sink caused by the back contact. Electrons recombining at the surface simply will not recombine in the bulk. The sensitivity in the notch can also be clearly seen.

While SRH recombination may not dominate bulk recombination, there is still room for improvement to efficiency. In total, additionally 2 % efficiency can be gained if SRH is completely nullified, with an increase of FF and V_{OC} of about 4 % (absolute) and 50 mV, respectively; however, this quantification depends greatly on the effectiveness of radiative recombination. The potential improvement to the back contact and front contact regions, optically and electrically, were also investigated. If back contact recombination is set low, an increase to V_{OC} of about 60 mV can be seen, but the maximum power point is not changed substantially, and thus, neither is the efficiency. For back graded Ga-profiles, the back contact recombination is practically rendered harmless, but with e.g. passivated back contact [103] another optimization point may well be found. Optically, the front contact, including the buffer layer and total reflection, constitutes about 4 mA cm⁻² improvement potential, or an equivalent 3 % efficiency, but to gain all of it is not realistic since the front layers are required to form a functioning device, and to have descent conductivity in the TCO there will always be some parasitic absorption from free carriers. Finally, by setting the series resistance and shunt conductance in the model to zero, a small absolute improvement of 1 % efficiency can be seen, by improving FF . For future work, if the back contact can be passivated and in addition be made optically reflective, the absorber layer can be thinned down and the efficiency increase due to, in part, a higher relative absorption in the SCR.

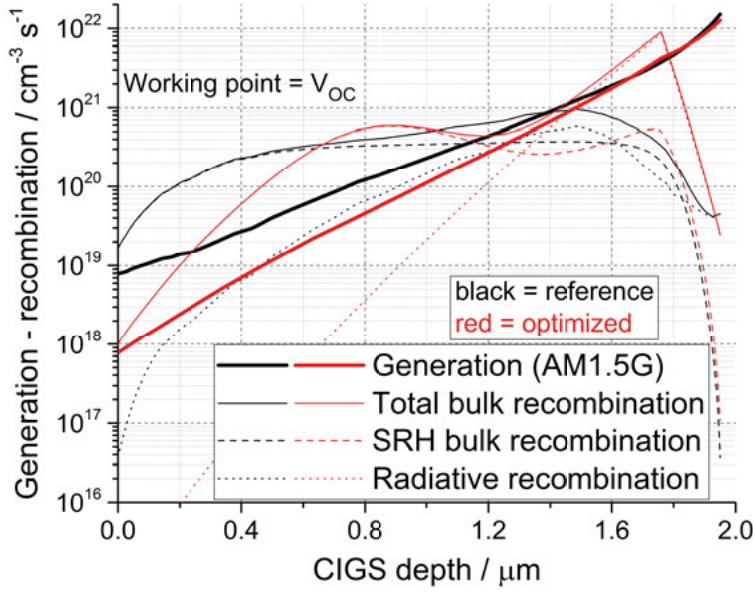


Figure 15. The bulk recombination in model B at V_{OC} , simulated using the EDS average profile (black colors), and the optimized DG Ga-profile (red colors). Apparent from the figure is that radiative recombination becomes a large limiting factor when the Ga-profile is engineered to minimize back contact recombination and interface recombination. Especially in the notch where there is a large accumulation of minority carriers.

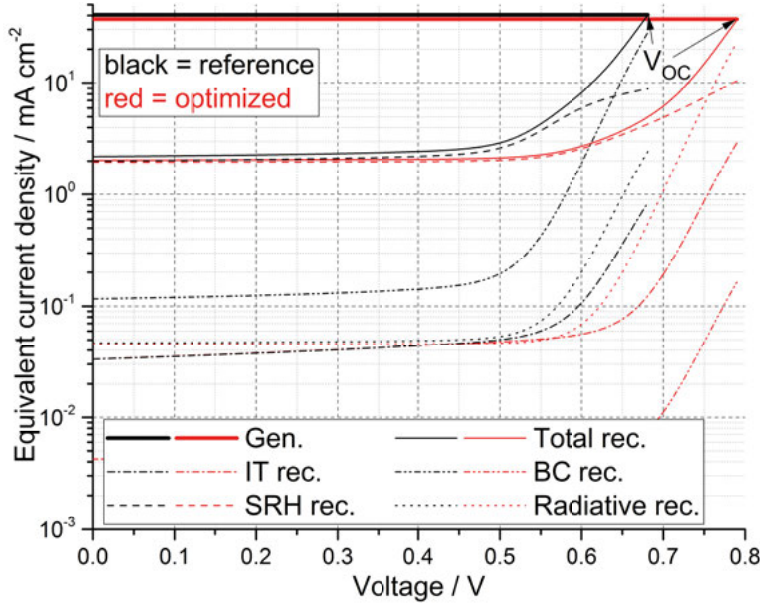


Figure 16. The recombination currents. In contrast to figure 15, the interface and back contact recombination are quantified. The reference model B (black) with EDS-determined Ga-profile is dominated by SRH bulk recombination for most part of the voltage range, but at voltages close to V_{OC} the back contact recombination dominates. The optimized Ga-profile in model B is instead dominated by bulk recombination for the whole voltage range, first SRH and close to V_{OC} radiative recombination. Back contact recombination is in effect passivated.

6.3 Absorption coefficient and bandgap narrowing in CZTS

A CZTS baseline device model was constructed in the study that constitutes paper II, which was done to obtain realistically quantified loss mechanisms. In the evaluation of the opto-electrical properties of CZTS films and devices, one clearly sees a discrepancy between absorption onset and electronic bandgap, as described in chapter 3. The broad sub-bandgap absorption, which is clearly observed in ellipsometry and R-T, appears not to contribute to carrier collection as seen from QE, where there is a distinct tail. In figure 17, this discrepancy is exemplified by QE simulations in SCAPS, by the use of differently obtained absorption coefficients, from ellipsometry [104], R-T [105] and calculations [106]. To circumvent this problem, for modeling purposes, a semi-empirical band tail was created by numerically extracting the absorption coefficient, as measured with R-T, from QE. Relation (28) is assumed to take the general form

$$QE(\lambda) = \frac{\int G(\lambda, x) f_c(x) dx}{\Phi_{in}(\lambda)} \quad (44)$$

where f_c is the collection probability at x and the generation function G in turn is, assuming Beer Lambert attenuation;

$$G(\lambda, x) = [1 - R(\lambda)] \Phi_{in} \alpha(\lambda) \exp[-\alpha(\lambda)x]. \quad (45)$$

The end result, as seen in figure 17 and used in the baseline model of paper II, is not necessarily reflecting the true absorption properties of CZTS, but in terms of device behavior, is the effective absorption coefficient that can be utilized in the device. To be clear; the tail of the experimental absorption coefficient does not cause a deficiency of the CZTS device performance, on the contrary; it may be seen as a property to enhance current generation. However, it is an indicator of imperfect crystal quality and, ultimately, will have a detrimental effect on the efficiency.

Taking potential fluctuation of the band edges into account [55, 107], a lower (uniform) electronic bandgap energy was used in the model, compared to theory, disjoint from the absorption coefficient. Best fit was achieved with a bandgap of 1.35 eV which correlates well with the main peak from PL around 1.35 eV [68]. Thus, the electronic bandgap is seen acting like a charge carrier percolation energy, where the electrons are free to move through the system at a lower energy compared to the nominal conduction band edge.

It is not known whether the sub-bandgap absorption originate from the same phenomenon that causes the low PL peak. Nevertheless, as was shown in paper II, the bandgap narrowing is causing a substantial V_{OC} -deficit of 150 meV, which is expected by (27) if one considers the nominal $E_g = 1.5$ eV. A

FF drop of 1.5 % was also seen with bandgap narrowing, resulting in more than 3 % total efficiency loss, as compared to a semi-ideal reference model, see table 3 in paper II and surrounding discussion for further details. Thus, we should strive towards making CZTS absorber layers with bandgap energies closer to the theoretical values, and one route is to mix same-octet elemental substitutes, e.g. Ge or Si to substitute Sn, or Se to substitute S, as previously discussed, into the absorber. In a study with different S/VI [61], it can be seen that the pure sulfide has a larger band tail in the Tauc plot compared to the sulfo-selenide mixes.

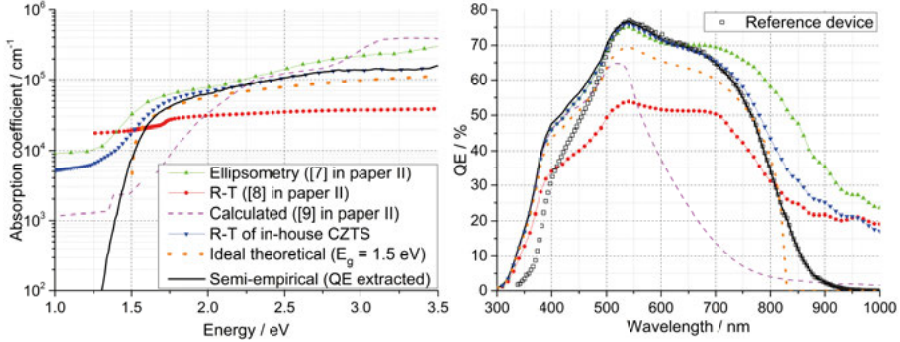


Figure 17. The absorption coefficients (left hand side) from literature, as calculated from the ideal square root dependence, similar to equation (33) and (34), and from extracting the absorption coefficient from QE based on the R-T measurement on an in-house sample. The impact on the QE simulations are clear (right hand side).

6.4 Reduction of interface recombination in CZTS

Apart from the bandgap narrowing, discussed in the previous section, several other loss mechanisms were identified and implemented in the baseline model, including interface recombination, based on J-V and QE characterization and fitting procedures. Table 3 in paper II summarizes these mechanisms and respective quantified efficiency loss. The activation energy obtained with J-V-T analysis, by using relation (27), was $E_A = 1.0$ eV. It matches the interface bandgap, as discussed in chapter 4, and it is well under the bandgap of the absorber, even when bandgap narrowing is considered. In the model, best fit was obtained for interface traps that manifests as a V_{OC} -deficit of about 300 mV and a total efficiency loss of almost 7 %, compared to a semi-ideal reference model. Moreover, interface recombination and bandgap narrowing losses were shown to be 1:1 cumulative with each other, in total manifesting as 10 % efficiency loss.

To improve the p-n junction interface the alternative buffer layer ZTO was deposited by atomic layer deposition (ALD), see paper III. It has been shown that one can control both electron affinity and bandgap by varying composition and deposition temperature [39], thus tailoring the buffer layer to be suitable for a wide variety of absorber layers. Different temperature

conditions and surface treatments were investigated and it was shown that $E_A = 1.36$ eV for the best ZTO device, with potassium cyanide etching and 95° C ALD deposition temperature, as compared to 0.98 eV for the CdS reference device. On average, V_{OC} improvement was in the order of 100 mV compared to the CdS references from the same batch. The improvement to V_{OC} in conjunction with the higher activation energy is a clear indicator that the interface recombination is reduced, and that the dominant recombination path even may have moved into the bulk for the ZTO device. Interestingly, later in-house studies with ZTO have shown great promise. In fact, although no certification was made, the world record-level Cd-free CZTS and Cu-GaSe₂ devices were made with ZTO, see paper 4 and 6 from list of related papers. In both cases V_{OC} -deficit was reduced greatly compared to their respective CdS reference.

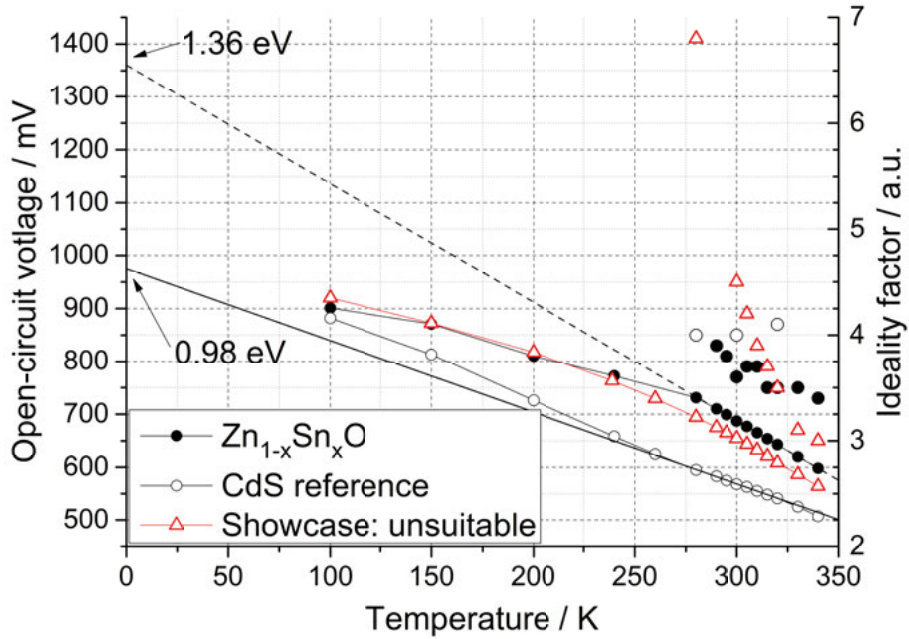


Figure 18. The $V_{OC}(T)$ extracted from J-V-T, and respective ideality factors for some of the temperature points. As an example, the red triangles seem to have a linear $V_{OC}(T)$ behavior around RT but the ideality factor has a strong temperature dependence which makes the analysis uncertain.

6.5 Collection length and doping concentration in CZTS

In paper V, an experimental study of the CZTS layer thickness was performed. Layers and devices with CZTS thickness between 0.5 μm and 2.0 μm were fabricated with nominal device composition. The absorber layers were analyzed with x-ray diffraction (XRD) and Raman, where both SnS

and ZnS secondary phases were observed in the films. Device characterization was performed with J-V and QE-V, see figure 19 for the characteristic J-V parameters. Experimentally, there was a step-like thickness variation for each J-V parameter comparing the two thinnest devices to 0.75 μm . This step may originate from a relatively large amount of phase segregation, in terms of volume fraction. Although scattered, FF showed no trend with varying thickness, but J_{SC} as determined from QE, and consequently; η , showed a trend to increase with increasing thickness. Results from J-V simulations of models with varying CZTS thickness, based on the baseline model in paper II, are consistent with the measurements, see figure 19. The insensitivity to absorber thickness, exhibited by V_{OC} and FF is attributed to a dominating interface recombination. The thinnest two samples are considered outliers. Even if the crystal quality of the CZTS itself, as determined from XRD, was found to be similar to the other devices, it is likely that such thin absorber layers are more sensitive to roughness and formation of secondary phases forming at the surfaces, since these will constitute a larger volume fraction. The discontinuity for the device parameters between 0.7 μm and 0.75 μm could not be reproduced by simulations with only absorber thickness variations in the model.

Good fits to the well-behaved samples were obtained with minority carrier diffusion length of 500 nm, as compared to 250 nm in the baseline model, which still is in the upper limit of the nominal range of plausible diffusion lengths, as can be seen from figure 4 in paper II. In the baseline model, SRH recombination causes the largest individual loss due to large J_{SC} and FF losses. In figure 19, a saturation of J_{SC} is seen at around 1.0 μm , which means that the current collection with 500 nm diffusion length is still sub-optimal. The variation with diffusion lengths of each J-V parameter was simulated in two models, with (model A) and without (model B) interface recombination, and the result can also be seen in figure 19.

While the diffusion length is important for current collection, back contact and interface recombination are playing important roles as well⁹, the majority of the total current collection is determined by interplay between diffusion length and the depletion width. In figure 20, QE simulations in SCAPS with varying doping and deep defect concentrations can be seen. The charge separation that takes place in the SCR due to the electric field will act more effectively with a wider depletion width. Thus, a lower doping concentration can be beneficial, and, in the case of thin film solar cells, it most probably is beneficial. The trade-off depends on the system; in the case of high quality crystalline absorber layers, with long minority carrier lifetimes, the sensitivity to W_D is lower than for an absorber with short lifetimes. Moreover, since the doping concentration also contributes to the built-in potential, it can theoretically enhance V_{OC} .

⁹ For very short diffusion lengths the back contact may even be invisible to carriers moving around in the quasi neutral bulk region further away from the back contact.

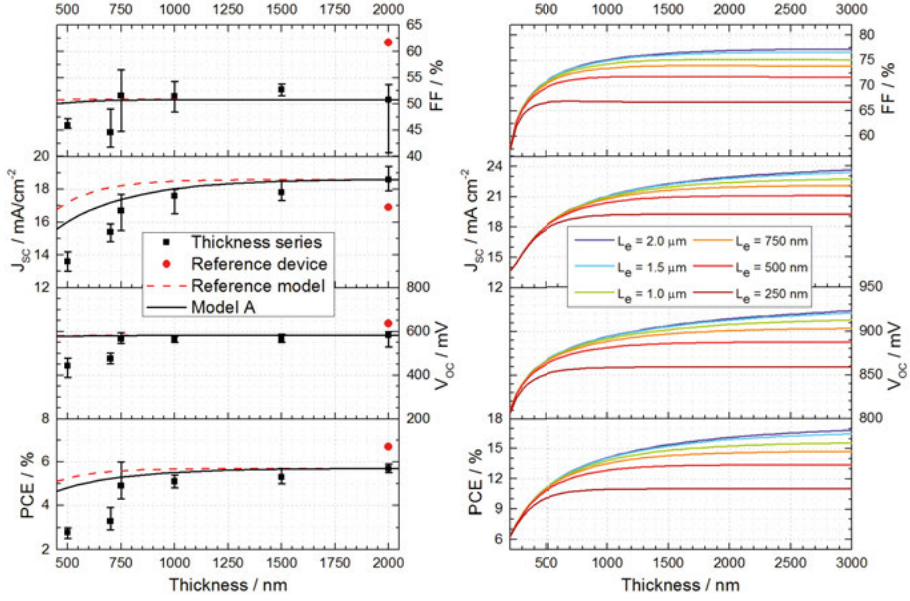


Figure 19. On the left hand side: The characteristic J-V parameters from the reference device in paper II (red dot), corresponding normalized reference model of paper II (dashed line), model A (solid line) pf paper IV, and the measured values from the thickness series (squares). In model A $L_n = 500$ nm, compared to the reference model with $L_n = 250$ nm. On the right hand side: The thickness variation trends in model B of paper IV. In this model, without interface traps, the saturation of FF and V_{oc} is pushed right, to thicker absorber layers.

To obtain a high quality CZTS absorber layer, preferably with long diffusion lengths, it is critical to control the annealing conditions, and avoid loss of S and Sn by having a high-sulfur partial pressure, and thus preventing volatile SnS formation. In paper VI, CuS capping layers were deposited on top of CZTS to investigate their ability to prevent absorber decomposition in the anneal step. Three conditions were varied, CuS cap or not, high- or low-sulfur partial pressure, and TiN back contact barrier layer nor not, in total 2^3 variations. Two variations exhibited nominal performance, the reference device and the TiN device without cap, annealed under normal conditions. The other devices had reduced J_{sc} , FF and V_{oc} to various degrees. From C-V and drive-level capacitance profiling, the apparent doping concentrations of every degraded device was of the order of 10^{18} cm⁻³. The reduction of J_{sc} is to be expected with such a high doping, since W_D will be almost negligible, compared to a nominal doping two order of magnitudes lower. Thus, the current collection would be decided by the diffusion length by itself. A high concentration of holes close to the interface is likely to enhance interface recombination which will reduce V_{oc} rather than enhance it as mentioned in the previous paragraph, especially if tunneling enhanced recombination is considered. A detailed discussion on the samples is available in paper VI, but as always with poor efficiency devices, there is a multitude of effects

that may degrade the performance; the worse device, the harder to pinpoint the exact reason behind it. It is evident that doping concentration is central to several properties of a thin film device, not only current collection. Nevertheless, for moderate variations of doping concentration around nominal values, current collection may be the property most affected by the variation, as illustrated in figure 19.

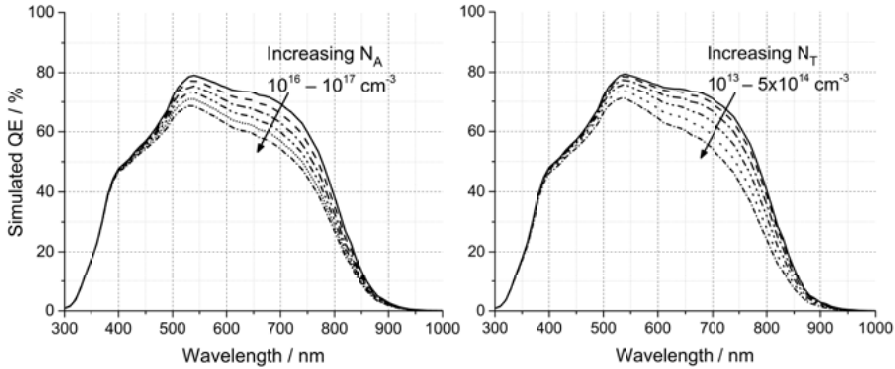


Figure 20. QE-simulation of a doping variation (left hand side) and deep defect variation (right hand side), both affecting collection of minority carriers. A small difference can be detected on the spread of QE at mid-range to long wavelengths, where the deep defects that shorten the diffusion length weights towards a lower collection at long wavelengths, and doping affects the QE curve on the whole more uniformly.

Extracting the doping concentration from C-V was employed in papers I, II and VI as means to strengthen models or arguments of the effects observed in respective study. Paper VII, on the other hand, is an in-depth study meant to provide a less ambiguous method for the extraction of doping from C-V. In the study, alternative structures with CZTS and ZnS between metal contacts were fabricated. CZTS itself seems to form ohmic contacts when deposited on Mo with Ni/Al/Ni as front contact, and as such, no capacitive method is viable on that sample. It does exhibit Schottky barriers at low temperature, and while not exploited in paper VII, it could be interesting for further investigation of the capacitive response of CZTS in the future. Nevertheless, ZnS was seen to show very low conductance and was chosen as a barrier layer in a CZTS/ZnS sandwich, or metal-insulator-semiconductor (MIS), structure. With (38) it was possible to extract the junction capacitance for CZTS, which exhibited a strong dependence on frequency. The frequency dependence is a strong indicator of deep defects being present. The MIS system was modeled in SCAPS, and from C-V simulations the best fitting doping concentration and deep defect concentration was extracted. A clear trend is seen in figure 21; that for low frequency a higher doping concentration and deep defect concentration is given, compared to moderate frequencies. Frequencies above the cut-off frequency (40), of the order 100 kHz, were not investigated. When compared to a device from a CZTS absorber

layer from the same batch, it was seen that the doping concentration from C-V may be underestimated down to a quarter of the more reliable value. A four times difference in doping will equal about two times difference in W_D , see (41), which will have a strong effect on the assumption of L_n . The doping of both the solar cell and MIS devices were high, of the order of 10^{17} cm^{-3} , and the uncertainty is in part due to that no n^+-p -type junction could be formed in the device with such high doping.

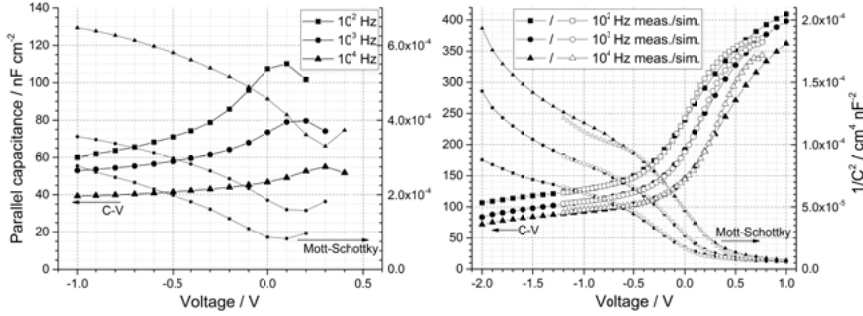


Figure 21. C-V and Mott Schottky plots of a reference device (left hand side) and of the MIS CZTS/ZnS structure including SCAPS simulations (right hand side). The doping concentration (shallow defects) is visible around 0 V, depending on the frequency.

6.6 Prospect of sulfo-selenium grading in CZTS

In a similar manner to the Ga-profile in CIGS, one can construct composition gradients in CZTS as well. There are many different variants where substitutions of elements are theoretically possible [108], as long as the octet rule is maintained, of course including S/VI, as defined in chapter 3. For this purpose, a CZTSSe device model was constructed. However, in comparison to the work done for the CZTS model in paper II, and in light of CZTSSe being a newer in-house process, the experimental data available is still limited, and e.g. J-V-T characterization on a CZTSSe with varying S/VI is yet to be performed. Moreover, as of yet no pure-selenium CZTSe has been created with the standard fabrication process, where sulfur is part of the precursor.

The key modeling parameters of pure-selenium CZTSe, that differ from the modeling parameters used in paper II to model CZTS, are; E_g , χ , ϵ , μ , N_A and α , see table 3. E_g was extracted from a mixed S/VI composition series, using relationship (34), but extrapolated linearly to S/VI = 0 using the bandgap bowing calculated with first principles [109]. The electron affinity was assumed to vary according to variation of the conduction band by first principle calculations [109], the relative permittivity according to [106], and the hole mobility was chosen in the middle range of reported values [110], and the electron mobility calculated with the assumption $\mu_p/\mu_n = m_n^*/m_p^*$ [22] with effective mass ratio taken from first principle calculations [106].

Moreover, based on in-house C-V characterization of the mixed S/VI series which exhibited no trend in apparent doping concentration according to (43), the doping concentration was set constant and independent of S/VI. Likewise, the deep defect concentration was set independent of S/VI which, in conjunction with the change in mobility, leads to a longer diffusion length $L_n = 280$ nm for the pure-selenide, compared to $L_n = 250$ nm for the pure-sulfide. The absorption coefficient was extracted from the mixed S/VI composition series using the same method presented in paper II, but shifted to fit $E_g = 0.96$ eV for S/VI = 0, see figure 22. The back contact work function, front surface reflection, series resistance and shunt conductance were all set to be independent on S/VI variation; The back contact was set to “flat band”, meaning a variation to maintain ohmic contact with the absorber layer, and as such being independent on S/VI variation. Series resistance, shunt conductance and front surface reflection are all considered to be of minor importance to the S/VI models. In addition, the simulations were seen to be insensitive to realistic variations of the back contact work function. Due to the interplay between μ and N_T , the value of the μ does not affect the effective L_n , see (15), for a particular composition. However, the variation of L_n as a function S/VI should be studied further with more rigorous electrical characterization. Any large change to N_A is unexpected for well-behaved devices, but should there be a difference one may expect that the optimized S/VI gradient will change as well, since the doping determines the depletion width and to some degree recombination at the interface. Finally, a change in α towards higher values will shift generation of minority carriers closer to the junction, and vice versa; such a change will also have an effect on the optimum S-profile.

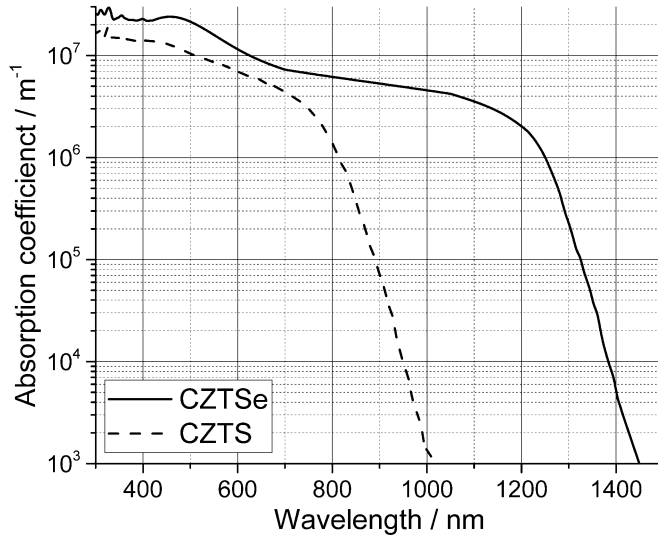


Figure 22. The absorption coefficients used in the CZTSSe model. In-between SCAPS interpolates the sulfo-selenide mix absorption.

Table 3. The key modeling parameters that were changed from the original model of paper II, including the difference between CZTS and CZTSe for these parameters.

Modeling Parameter	CZTS	CZTSe	Δ / %
E_g / eV	1.35	0.96	-29
χ / eV	3.90	4.18	7
ε	6.7^{10}	8.5	27
μ / $\text{cm}^2 \text{V}^{-1} \text{s}^{-1}$	26	34	31
N_A / cm^{-3}	$2.6 \times 10^{16}^{11}$	2.6×10^{16}	0

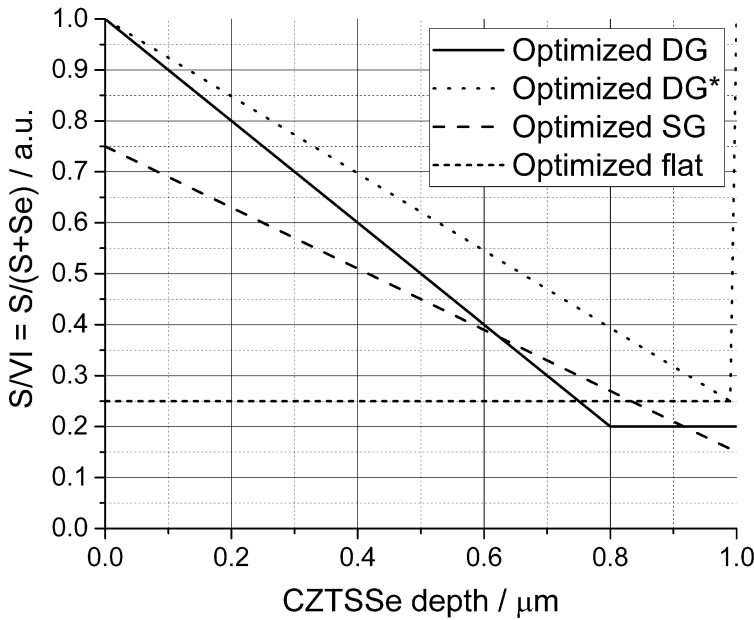


Figure 23. The optimized S-profiles in the CZTSSe model. The flat profile can be used as a reference point.

All in all, the results presented herein will give a general idea on the prospect of S-profile optimization for current in-house devices and future devices. In fact, it is our hope that the material quality of future fabricated kesterite absorber layers will increase to such an extent that a reevaluation of the S-profile optimization is required.

In figure 23, the optimized DG, SG and flat S-profiles are shown, and in figure 24 the simulated J-V data including efficiencies for corresponding profiles are presented. The notch of the DG was restricted from being closer than 200 nm to the interface, in the same manner as for the Ga-profile opti-

¹⁰ Altered from $\varepsilon = 6.5$ used in paper II.

¹¹ Altered from $N_A = 2 \times 10^{16} \text{ cm}^{-3}$ used in paper II.

mization in paper I. The extremes, CZTSe and CZTS, were not created to fit specific devices, but the general efficiencies correspond well to the upper end of in-house experimental values obtained so far. The average S/VI of the optimum S-profiles were also modeled as a uniform level for reference, but the optimized flat S-profile is considered the best reference point, in part since optimum flat profile may be of interest by itself, since creating any S/VI gradients have been shown challenging [111].

First, it is observed that S-grading in CZTSSe can in fact lead to improved device performance. Compared to highest uniformly graded CZTSSe, with $S/VI = 0.25$, see the flat S-profile in figure 23, approximately an additional 1 % efficiency is yielded with a DG S-profile, and +0.8 % with a SG S-profile. If the notch position restriction is removed, 0.5 % extra efficiency can be gained, but the yield from a 10 nm steep S/VI front grading may remain hypothetical due to limitation in fabrication control, and inter-diffusion of atoms over time. In figure 25, the recombination partition is presented at J_{SC} (left hand side) and V_{OC} (right hand side), normalized for total recombination. Included are the absolute recombination currents, shown as numbers for each significant part. Interface recombination plays an insignificant role to the limit of J_{SC} , where bulk recombination dominates in all cases, and back contact recombination plays a minor part for CZTSSe with uniform composition. At V_{OC} , the role of the interface becomes important; as expected for the case of CZTS and CZTSe, interface recombination dominates the prior while it has a minor effect on the latter. However, it is interesting to note that in all realistic cases of S/VI grading, interface recombination still influence the limitation to V_{OC} substantially, both in relative and absolute numbers. Two effects are identified as majority influence on V_{OC} -deficit: 1) A negative CBO towards the buffer layer generally limits the quasi Fermi level splitting at the interface. However, quasi Fermi level splitting at the absorber side of the interface is influence by bulk bandgap, meaning that the front grading will introduce a relative V_{OC} -deficit reduction. The minimum bandgap ($E_{g,min}$) in the vicinity of the junction normally sets the limit to quasi Fermi level splitting, which means that a front graded conduction band in practice does not add to the V_{OC} -deficit, despite increasing cliff-type band alignment. On the other hand: 2) Bandgap widening towards the interface will reduce interface recombination if the limiting charge carrier concentration at the interface can be reduced. In the cases of these simulations, it is the hole concentration. The V_{OC} -deficit, as calculated from the $E_{g,min} - V_{OC}$, are seen in table 4 along with the characteristic J-V parameters. The interesting fact that the interface recombination current increases, both in relative and absolute terms, with decreasing front surface S/VI composition is then related to the hole concentration at the interface. The opposite trend is seen for the V_{OC} -deficit, which does increase with increasing bandgap, related the limitation to quasi Fermi level splitting.

The benefits of the back grading is straightforward; it is a trade-off between generation and enhanced collection due to the quasi electrical field, i.e. the conduction band grading, that increases the effective L_n , and acts as a passivation of the back contact. For larger L_n in pure-selenium kesterites, the trade-off would be more in favor of lower S/VI.

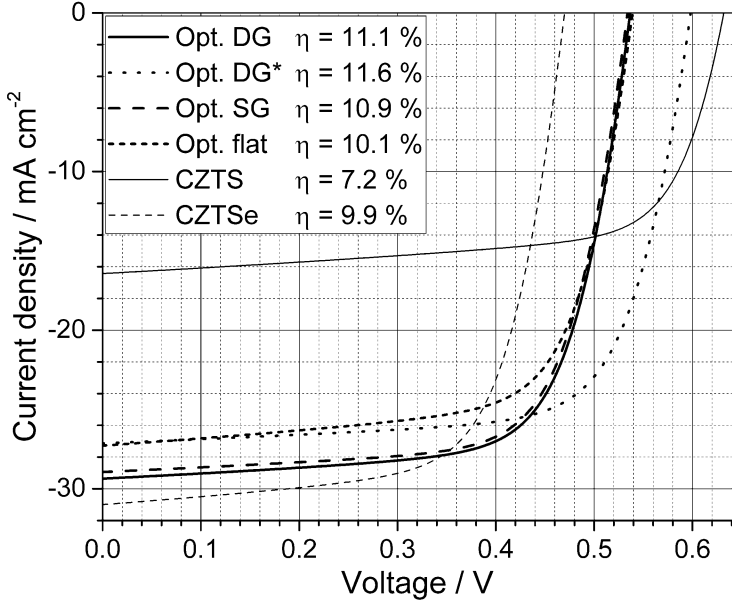


Figure 24. Simulated J-V curves of the optimized S-profiles in the CZTSSe model, including the pure-sulfide and pure-selenide models.

Table 4. The characteristic J-V parameters and V_{OC} -deficit as calculated from the minimum bandgap in the S-profile. The efficiency can be found in figure 24.

Model	J_{SC} / mA cm ⁻²	V_{OC} / mV	FF / %	η / %	V_{OC} -deficit / mV
Opt. DG	29.4	537	77.2	11.1	493
Opt. DG*	27.1	598	71.3	11.6	442
Opt. SG	28.9	534	70.6	10.9	472
Opt. flat	27.3	540	68.9	10.1	501

Thus, S/VI grading CZTSSe and optimizing the S-profile will contribute to an increased efficiency, but will not reduce the current limitations of kesterite solar cells enough to enable commercialization. However, if S/VI gradients can be realized, the S-profile optimization in conjunction with an alternative buffer layer, such as ZTO used in paper III, would bring CZTSSe a substantial bit closer. If, as previously discussed, ways to reduce bulk recombination losses are found, the next logical step will be look into the back contact.

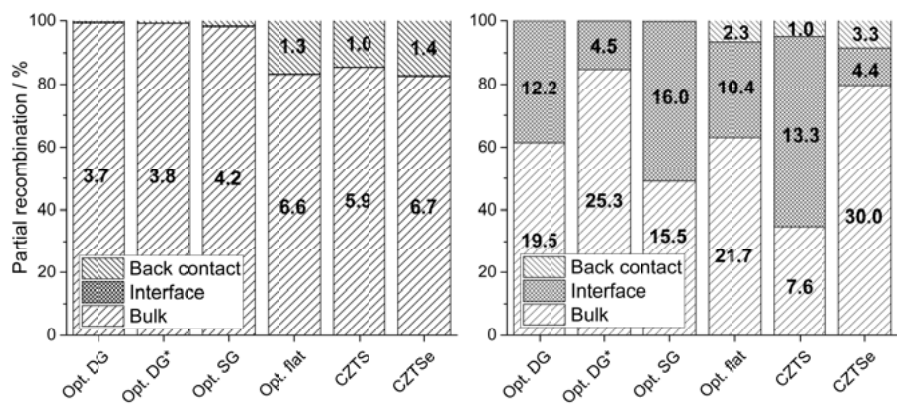


Figure 25. Simulated recombination currents at J_{sc} (left hand side) and at V_{oc} (right hand side), with normalized stacked columns (y-axis), and absolute values (numbers) in mA cm⁻².

7. Concluding remarks and outlook

In this thesis, research has been done on thin film $\text{Cu}(\text{In,Ga})\text{Se}_2$ (CIGS) solar cells and its sibling thin film $\text{Cu}_2\text{ZnSnS}_4$ (CZTS) solar cells, using optoelectrical characterization and device modeling as tools to further our understanding of loss mechanisms and how to improve upon the device efficiencies. The modeling is used to bridge between theory and experiment, allowing better analysis of experimental results, as well as prediction losses to guide improvement on experimental devices.

CIGS technology has had a few distinct efficiency leaps in the last few years. In part of this thesis, device models with different defect characteristics were created, based on a $>19\%$ efficient CIGS device with known compositional Ga-profile, to see how much the efficiency could be further increased by optimizing the Ga-profile. Both single graded and double graded Ga-profiles were modeled, and a general efficiency improvement, from a nominal 19.5% to up to 21.4% maximum efficiency was seen for an optimized double graded Ga-profile in one of the models. The best single graded Ga-profile in the same model yielded 20.8% efficiency. With such high efficiencies, the minority carrier diffusion length is of the same order of magnitude as the thickness of the device, meaning that the back contact, and its role as electron sink, strongly influences the performance of the device. With a back grading, the diffusion towards the back contact can be reduced, in effect passivating the back contact. The front grading, which is a part of the double graded Ga-profiles, instead means that the quasi Fermi level splitting can be increased in the junction, and moves part of the generation into the absorber and away from the detrimental interface. In effect, the open-circuit voltage (V_{OC}) is allowed to be higher for the double graded model compared to the single graded model, with a small hit to the fill-factor (FF). In the case of no interface traps between the CIGS absorber and CdS buffer layer, the efficiencies in the single graded models were similar to the double graded models. This exemplifies the effect of having a graded composition in the absorber layer, as it is meant to redistribute generation and recombination such that it becomes more beneficial for solar cell device performance. The losses for the optimized models were also investigated. It was seen that, despite the long diffusion length, defect assisted recombination still contributes to about 2% absolute loss of efficiency, while the majority of the bulk recombination is radiative recombination. Another 3% efficiency can be gained if optical properties of the stack are optimized, i.e. increasing the

generation by minimizing both front surface reflection and parasitic absorption. Finally, if one can avoid losses due to series resistance and shunt conductance, a further gain of about 1 % in absolute efficiency can be achieved.

Compared to CIGS, the CZTS technology for thin film solar cells is less mature and there is still a plenty of room for improvement. The pure-sulfide CZTS solar cells, which were of major focus in this thesis, have been shown to suffer from interface recombination, bandgap fluctuations, and poor collection. By modeling and quantification of each individual contribution to performance deficiency, it was seen that interface recombination constitutes the largest part of V_{OC} -deficit with as much as -300 mV. An experimental study with $Zn_{1-x}Sn_xO$ (ZTO) replacing the standard CdS as buffer layer shows that the interface recombination can be reduced. In effect, about 100 mV in V_{OC} was gained, and the increase comes in conjunction with a higher activation energy for the dominant recombination mechanism, from a nominal 1.00 eV to 1.36 eV, indicating a reduced interface recombination as well. However, bulk recombination was the most detrimental current loss mechanism in the standard CZTS device, and obviously will remain as such even for well-suited alternative buffer materials. In fact, in a thickness study it was seen that the collection depth of minority carriers, i.e. sum of depletion width and effective diffusion length, is so short that absorber layer thickness above 1 μm is redundant. This is affected by a detrimental interface and bandgap fluctuations as well, and if these could be improved upon, then the efficiency would improve with thicker absorber layers.

Parts of the results in this thesis are quite general; simulating a trend may trump the importance of having every device model parameter accurately quantified. However, to obtain reliable results from modeling, one should take care in quantifying and fixing as many parameters as possible. Any unknown parameter becomes an additional free parameter, and as such the space of uncertainty grows larger. Thus, a large part of this study has been dedicated to quantify the interplay among the absorption coefficient, effective diffusion length and doping concentration of CZTS, each contributing heavily to the solar cell performance. The apparent doping concentration is usually extracted from electrical measurements where the capacitance is characterized with an equivalent circuit model. As part of this thesis, the capacitance-voltage (C-V) characterization, and its use on CZTS absorber layers, was studied in an alternative structure, with ZnS as a barrier layer instead of the regular front stack of CdS, i-ZnO and ZnO:Al. Due to deep defects in the CZTS material, it becomes important to select an appropriate measurement frequency for C-V characterization. In addition, by comparing a regular device with the alternative structure, it was seen that the doping concentration could be substantially underestimated if C-V is done on the regular device stack. This can, in turn, lead to misjudgment of e.g. the diffusion length. Uncertainty of extracting the doping concentration from C-V increases with increasing doping concentration, due to failure of the one-sided junction approximation. High doping concentration $\gg 10^{16} \text{ cm}^{-3}$ may

also lead to degraded solar cell performance, and therefore, having a doping concentration of around 10^{16} cm^{-3} in the thin film absorber layers is preferable. In general, if CZTS derivatives with higher material quality can be fabricated, e.g. without high density of detrimental defect complexes, it is plausible that opto-electrical characterization will be easier, and as such, the construction of an accurate device models as well.

Finally, a sulfo-selenide $\text{Cu}_2\text{ZnSn}(\text{S},\text{Se})_4$ (CZTSSe) model was created to study the prospect of S/(S+Se) gradients in the absorber, much like a Ga-profile in the CIGS. It is seen that an improvement of about 1 % efficiency can be gained as compared to highest efficiency with uniform S/(S+Se) = 0.25. Experimental research on the in-house CZTSSe device fabrication process is undergoing, and characterization of these devices has so far been limited. Hence, some of the parameters in the CZTSSe remain uncertain, but preliminary modeling suggests that the chosen parameters have been quantified within the ballpark values of the experimental devices. Only drastic changes to these parameters would lead to drastic changes in simulations.

For future work, to improve the already high CIGS solar cell efficiency it is suggested that alternative front contact layers are investigated, e.g. high mobility transparent conductive oxides, to reduce the parasitic absorption. If series resistance can be reduced simultaneously, it will add to the improvement. Additionally, passivation of the back contact with a reflective barrier layer should allow for thinner devices which will shift the generation and recombination profiles to benefit the efficiency. At that point, one should consider re-optimizing the Ga-profile for such a device.

For CZTS and its derivatives, a combination of alternative front layers, elemental substitution and an optimization of the absorber layer fabrication process are needed to reach commercially competitive device standards. S/(S+Se) gradients alone, at this point, are not enough to bring CZTSSe to that performance level. In-depth analyses for future work on CZTSSe should include temperature dependent current-voltage for activation energy and ideality factor extraction, and temperature dependent admittance spectroscopy and C-V to evaluate the apparent doping concentration, possibly using ZnS as a barrier layer on top of the absorber. In addition, an experimental series using ZTO buffer layers with varying bandgap could add valuable information about in-house sulfo-selenide interfacial properties.

In terms of modeling in general, present limitation in our understanding is in part related to the fact that SCAPS is restricted to 1-D. Optical effects from surface roughness and interference, as well as electrical effects such as a laterally varying space-charge region, bandgap fluctuations and grain boundaries; all may affect our current interpretation of the device behavior. In practice, these 2-D and 3-D effects will probably not overturn our current understanding, but will nevertheless be of interest for future research.

Sammanfattning på svenska

Denna avhandling omfattar forskning på två typer av tunnfilmsolceller, Cu(In,Ga)Se_2 (CIGS) och $\text{Cu}_2\text{ZnSnS}_4$ (CZTS). Benämningen *tunntfilm* kommer av att båda dessa material har hög förmåga att absorbera ljus, vilket innebär att de kan göras mycket tunna utan att det medför väsentliga optiska förluster. Generellt är absorptionsskiktet i en tunnfilmsolcell av storleksordningen $1\text{ }\mu\text{m}$, vilket är ca. en hundradel så tjockt som konventionella kristallina kisel-solceller (c-Si). Standardsstrukturen för CIGS och CZTS utgörs av en metallisk bak-kontakt på ett substrat (vanligtvis glas), med absorptions-skiktet deponerat på bak-kontakten och påföljande tunna lager av CdS, intrinsiskt ZnO, och högdopad ZnO som utgör kontakten på framsidan. Fördelar med CIGS och CZTS jämfört med de etablerade c-Si-teknologierna är bl.a. snabbare, mer flexibel och kostnadseffektivare produktion, vilket i slutändan innebär en kortare återbetalningstid.

Marknaden för solceller ökar stadigt men är fortfarande småskalig med tanke på den stora potential som finns för solenergi. Varje år strålar genomsnittligen ca. 7000 gånger mer energi in från solen, jämfört med vad mänskligheten gör av med, enligt 2014 års statistik! Vad gäller samtliga solcellsteknologier är det långsiktiga målet att öka verkningsgraden, så att större del av mängden energi som strålar in från solen kan omvandlas till elektrisk energi. För att nå målet behövs en djup förståelse för både de grundläggande mekanismerna i en solcell och de praktiska moment som krävs för att tillverka en solcell. Sålunda omfattar forskning på solceller både teori och experiment, och som brygga mellan dessa kommer modellering in i bilden. Genom att numeriskt beräkna de fysikaliska tillstånd som råder för solcellerna, i en given struktur som definieras i modellen, kan man simulera fall som liknar praktiska experiment.

I denna avhandling användes modellering och elektrisk karakterisering som verktyg för att öka vår förståelse om de begränsningar och potentiella förbättringar som kan göras för CIGS och CZTS. Störst tyngd i arbetet ligger på CZTS, som fortfarande är i ett stadium där stora förbättringar behövs för att göra teknologin kommersiell. För modellering har programmet SCAPS (Solar Cell Capacitance Simulator) använts som är skapat för att simulera karakteristik som ström-spänning (J-V), kvanteffektivitet (QE), kapacitans-spänning (C-V) och admittans (Y), och i avhandlingen har primärt de två förstnämnda används.

Till följd av många års utveckling och forskning på CIGS har teknologin i dagsläget nått verkningsgrader över 22 %. Det är många faktorer som spelat in, substrat som används för solcellen, deponeringsprocess för absorptions-skiktet, optiskt och elektrisk optimering av framkontakt m.m. Som en del i denna avhandling konstruerades flera modeller i SCAPS med olika defekt-konstellationer, baserat på ett referensprov med 19,2 % verkningsgrad. I modellerna undersöktes den optimala sammansättningen av Ga mot In i CIGS som funktion av tjocklek, en sammansättningsvariation som brukar kallas Ga-profil, där ökad $GGI = Ga/(Ga+In)$ ökar bandgapet. Modellerna fastställdes genom att manuellt anpassa bl.a. defektkoncentrationen i CIGS så att J-V- och QE-simuleringar överensstämde med experimentell data från referensprovet. Sedan varierades enkel- och dubbelgraderade linjära Ga-profiler för att optimera verkningsgraden. Optimerade Ga-profiler medförde en genomsnittligt ökad GGI i CIGS, från $\langle GGI \rangle = 0,23$ till $\langle GGI \rangle \approx 0,4$, och upp till 2 % absolut ökning av verkningsgraden, högst med dubbelgraderad Ga-profil. En generell ökning av verkningsgraden med en ökande GGI-gradient mot bak-kontakten kunde ses för både enkel- och dubbelgraderade Ga-profiler. Denna ökning beror främst på att diffusion mot bak-kontakten kan minskas med hjälp av det kvasielektriska fält man får med bakgrade-ringen, och därmed minskar även förluster via rekombination vid bak-kontakten. För solceller med hög verkningsgrad är diffusionslängden lång för elektroner, vilket resulterar i att ytor kan bli en begränsande faktor då dessa blir synliga för elektronerna. Ytterligare en ökning av verkningsgraden kunde fås med en framåtgradient för de dubbelgraderade fallen, där en ökning av spänning erhålls med hjälp av bandgapsvidgning vid gränsskiktet, samt en omstrukturering av generation och rekombination i p-n-övergången. Vidare, bortom en optimerad Ga-profil, visar modellering på störst förbättringspotential med ca. 3 % absolut ökning av verkningsgraden genom minskade optiska förluster, framför allt parasitisk absorption och minskad totalreflektion, samt ca. 2 % ökning genom minskad bulkrekombination via djupa defekter.

För CZTS skapades i denna avhandling en grundmodell för att uppskatta fördelningen av de olika förlustmekanismerna. Modellen var baserad på ett standardprov med 6,7 % verkningsgrad, och anpassades efter J-V och QE data från referensprovet. Diffusionslängden för elektroner fastställdes till 250 nm med jämförelse av simulerad och experimentell spänningsberoende QE och J-V, tillsammans med en semi-empirisk anpassning av absorptionskoefficienten. Jämfört med en icke-begränsande diffusionslängd motsvarar 250 nm ca. 9 % total förlust (i frånvaro av andra förluster). Det finns emellertid en viss osäkerhet i diffusionslängden, och därutöver förväntas den förändras något beroende på tillverkningsprocessen av absorptionsskiktet. I en studie med tjockleksvariation av absorptionsskiktet passade en modellerad diffusionslängd på 500 nm bättre överens med experiment, vilket ligger inom osäkerhetsintervallet. Vidare utgjorde temperaturberoende J-V en stor del av studien för att undersöka dominerande rekombinationsvägar i CZTS.

Två metoder användes och jämfördes. Den första är en numerisk metod där aktiveringsenergin för den dominerande rekombinationsvägen itereras fram, utifrån temperaturvariationen av mättnadsströmmen och idealitetsfaktorn för solcellen. Den andra metoden bygger på ett uttryck för öppenkretsspänningen (V_{OC}), där man använder värden på temperaturen för vilka idealitetsfaktorn inte varierar. Båda dessa metoder pekade mot en generellt lägre aktiveringsenergi $E_A \approx 1$ eV jämfört med bandgapet för CZTS, $E_g \approx 1,5$ eV, vilket tyder på ett begränsande gränsskikt mellan CZTS och CdS. Den sistnämnda metoden, där V_{OC} används, ansågs vara mer robust så länge idealitetsfaktorn inte varierar med temperaturen. Om man därutöver tar hänsyn till bandgapsfluktuationer från defektkomplex i CZTS, som verkar sänka bandgapet till $E_g = 1,3-1,35$ eV, blir kombinationen med ett ofördelaktigt gränsskikt en total verkningsgradsförlust om ca. 10 % absolut. Genom att byta ut CdS till ett bandgapsanpassat $Zn_{1-x}Sn_xO_y$ höjdes aktiveringsenergin till $E_A = 1,36$ eV, och ett högre värde på V_{OC} erhöles, jämfört med en referens med CdS. Den semi-empiriska anpassningen av absorptionskoefficienten gjordes med utgångspunkt av experimentell absorptionskoefficient och gjordes för att anpassa främst koefficienten vid långa våglängder, nära bandgapet. Metoden bygger på antaganden om både diffusionslängd och dopningskoncentrationen i absorptionsskiktet, eftersom koncentrationen avgör hur stark bandböjning är, och därmed hur långt det elektriska fältet når. Med andra ord avgör dopning till stor del hur effektiv uppsamlingen av elektroner är, och som visats i denna avhandling kan en hög dopningskoncentration kraftigt sänka bl.a. kortslutningsströmmen. Vidare får koncentrationen utslag på den anpassade absorptionskoefficienten och på diffusionslängden, vilket gör att dopningen är en av de mest centrala parametrarna för att nå en bättre förståelse om absorbatorns egenskaper. Vanligtvis extraherar man dopningskoncentrationer från C-V analys på hela solceller. I en studie på alternativa enklare strukturer deponerades ZnS på direkt på CZTS, istället för CdS, och ZnO. ZnS är en isolator och förenklade analysen av CZTS. Det visade sig att valet av frekvens är avgörande för vilken dopningskoncentration som extraheras med C-V analys, på grund av djupa defekter som svarar på frekvensen vid vilken man mäter. Idealfallet är att mäta vid högre frekvens, där djupa defekter inte kan svara på modulationen, alternativt vid lägre temperatur där energin för att aktivera djupa defekter blir för låg. Dessvärre svarar dopningen i CZTS på liknande vis, vilket gör att det är svårt att särskilja på dopningskoncentrationen och koncentrationen av djupa defekter. Med ZnS deponerat på CZTS kunde en kapacitiv signal mätas, och systemet modelleras i SCAPS för att extrahera en mer exakt dopning. Denna metod visar att det är möjligt att underskatta dopning när man mäter C-V på hela solcellsstrukturer, speciellt om dopningen i absorptionsskiktet är hög, och att vidare användning av enklare system med ett barriärlager i form av ZnS är av intresse. Till sist har en modell med både $Cu_2ZnSnSe_4$ (CZTSe) och CZTS konstruerats för att undersöka huruvida $S/(S+Se)$ gradienter potentiellt kan öka verkningsgraden i en mix (CZTSSe), likt studien på optimerad Ga-profil som nämndes tidi-

gare. Med ett bandgap på $E_g \approx 1,0$ eV, något högre mobilitet samt mer gynnsam övergång via ledningsbandet till CdS gav J-V simuleringar med CZTSe-modellen högre verkningsgrad (9,9 %) jämfört med CZTS-modellen (7,2 %). Den bästa mixen utan gradient erhöles för $S/(S+Se) = 0,25$ vilket gav en verkningsgrad på 10,1 %. Optimerad dubbelgradient gav ytterligare ca 1 % i verkningsgrad, främst med minskad rekombination via bak-kontaken och bättre uppsamling, tack vare en bakåttgradient, med stigande $S/(S+Se)$ mot bak-kontaken. Dessa storleksordningar på förbättringar är dock inte tillräckligt för att ta CZTS till kommersiell nivå, förbättring på alla fronter är därav nödvändigt för att ta CZTS och CZTSSe till kommersiella nivåer.

Därmed kan det konstateras att modellering som verktyg för att analysera experimentell data möjliggör en djupare förståelse om de fenomen som utspelar sig i solcellerna. Därutöver kan det användas för att förutse möjliga vägar till förbättring, som visats i denna avhandling.

Acknowledgements

According to my grandparents, as a young kid I wanted to become a professor “when I got old”. Although I do not recall this wish, I am so grateful for have gotten the opportunity to get at least halfway there (depending on how you measure). Science and an overall curiosity have always been important to me, and despite (or maybe thanks to) the hardships involved with the Ph.D. studies, the last five years have been an amazing journey. Of course, I could not have done it, and I would not have had much fun doing it, without some important people around me!

Lotten, first of all; thank you for believing in me in the first place! It goes without saying that none of this would have been possible without you. I admire your intellect and I could truly not have had a better supervisor. Thank you for enduring the way my mind wanders and for being able to follow my distracted thoughts. Moreover, when I came to you with personal matters you showed me support and sympathy. It has been a truly enriching experience, and I wish you continued success within and without academia.

Jörgen, the first thing you said to me was asking if I had all my courses done to complete my master studies. It has only been downhill from then. No, not figuratively, but actually literally – in Åre! There are many things I am thankful for, not least the excellent supervision all matters of electrical characterization. But I really need to thank you for ~~lending~~ giving me the power lifting belt, all the nice stories and conversations about working out in all manners of sports. I hope you never lose your passion for sports and competition.

Marika, thank you for being such a pleasant person, keeping the big solar cell group together, and for the yearly ransom of apple mash (äppelmust).

Uwe, I don’t not know what the group(s), and students, would have done without you. I have really enjoyed your company, at and off work, with or without beer!

Bagge, thank you for endure my many silly problems with computer software and hardware!

Thanks to all the people in the **CZTS group**, the “veterans” like **Ray**, **Tove**, **Shu-Yi** and **Jes**, and the newer additions to the group **Nils**, **Katharina**, **Volodymyr**, **Sven**, **Alexandra**, **Svante** and others, for making the working environment better. Special appreciation to **Ray**, for your smiles and compliments, and for honoring me with the toastmaster title at your disputation party, I hope to see you in China... and **Tove** for being such a lovely person and neighbor, hope we meet in Gothenburg at some point!

Piotr, thank you for being who you are. I admire your ability to “cut through the BS” and I appreciate the times of discussion of all topics related and unrelated to work. Also, thanks for the nice stay in Warsaw! I hope our paths cross again in the future, who knows, maybe online in the crosshairs.

Lars and **Bart**, two of only a few people I know that really appreciate running and beer, and preferably one after the other. It has been fun hanging with you guys! Good times both south of Oxford and in New Orleans, and countless other times! Remember, 10 k around 40 as long as it is possible!

Lukas, we haven’t spent that much time together but the times we did, I’ve had really good times. Hope there will be more occasions for pool and alt-bier. So far, yours was the best!

Johan, thanks for being so nice travel company in Taiwan, and an excellent desk mate (despite all the calls), and early on for setting the standard for running in the division.

Pedro and **Viktor**, thank you for getting me started on something great!

The lunch gang (**Malkolm**, **Patrik**, **Asta** and others). Thanks for all the nice, interesting and weird discussions on the lunches. On so many occasions, it goes beyond counting. I’ll miss it. A shout out to **Malkolm** and **Patrik** who gave me so much support in the end.

Ingrid, thanks for conveying the feeling of security when first coming here, just knowing that you were here helped a lot!

A general thanks to **Shi-Li** and all the people in the people that maintain the division and make floor 1 in house 2 such a nice working place. Additional thanks to **Apurba** for making my thesis better.

Friday beer club – It’s genius! Especially for a sleep deprived and lost Ph.D student.

Café Ångström and **Jalla (Matverkstaden)** for providing the coffee @14.30!

Niklas and **Robert**, thank you for the greatness that is Crossfit Vanheim, a place for hard work, laughter and personal development. A place where one hour easily turns into three hours. Thanks to all the Vaner making the place the nicest box around. I will not stop at 400 kg!

Furlani och the gang at Chalmers; this is old news but I am still grateful for getting me started on this journey.

Westman, thanks for talking me into searching this position in the first place. It happened at Andra Långgatan i Göteborg, two or three days before last application date.

Sofia, thanks for the happy thoughts and support via the magic that is the Internet. It was worth a lot those mid-night hours of writing!

All of the **Siljevalls** (and one **Andersson**) for bringing so much outside perspective into my life, it was enriching to know you all. Also, thanks for all the food and good company! Wish you all the best for the future!

Christian and **Staffan**, my very best friends! It even feels like it's more than that... and of all the things have achieved in life, nothing beats still having you in my life.

Thanks to the **Kragner** family who offered respite in Malmö and Hjärlup. **Sister**, I will always be your little brother. And lovely little **Max**, who took me by storm, thanks for reminding me that when some things end, other begins. You may always call me Totte <3

Mom and **Dad**, there are no words to describe how thankful I am... for everything! I love you! Nuff said!

Did I miss anyone? Please refer to the last sentence on page 75!

Christopher Frisk
Uppsala, 26 April 2017

Appendix A

This appendix is dedicated to part of the numerical analysis that was used in the thesis. To analyze experimental data by applying the theory mentioned in chapter 4, a multitude of software programs can be used. In most studies, Origin Lab was used, which conveniently handles column based arithmetic and can be semi-automated with user-defined macros and import filters. However, for large sets of data, such as temperature dependent characterization, the analyses might be better suited in a matrix based arithmetic's tool such as MATLAB.

A.1 Loading large sets of data from J/C-V-T

To effectives the numerical problem solving, here is a short example on how to fast load a large amount of data in MATLAB, without having to manually copy and paste files, or data in files. The example is given for *.dat* files with the name on the form *[X][Y][Z][IVD][123K].dat*, where X, Y, and Z, that would stand for sample name, date and time, respectively, are not used. *[IVD]* marks a dark J-V measurement. The format is based on the output of the J/C-V-T set-up used at Ångström that through the years have not been connected to the Ångström Solar Cell group server and database.

First, we want to load the correct files, in this case the dark J-V measurement files, from a folder called *foldername*. Second step is to extract the temperature specified in the file name. Finally, we are loading the data into a struct called *data*, jumping over two empty rows since “we know” they are filled with text output from the measurement set-up. The functions in MATLAB can easily be found by searching for them via the built-in search function, or via the web.

```

>%Loading file names, not data itself
>files = dir([foldername '\*[IVD]*.dat']);
>
>%Enabling the extraction of temperature! Any digit
specified in [], and in >%any amount "+"
>%Then we remove the matching 'K' to make it a double
>expression = '[1234567890]+K';
>switch isempty(files)
>    case 1
>        disp('No mathing foldername or J-V data in
folder')
>        return;
>    case 0
>        T =
>str2double(strrep(regexp([files.name],expression,'match
'),'K'],''));
>end
>
>for i = 1:length(T)
>%Loading data (ascii) with dlmread. The two last argu-
ment specify to jump
>%two rows down, and zero columns in.
>    data(i).T = T(i);
>    data(i).JV = dlmread(fullfile(foldername,
files(i).name),'\t',2,0);
>end

```

The script above can be tailored for any data importation, and is extremely useful for large data analyses when automatic data retrieval via a server is not possible, such as from JCVT.

A.2 Temperature dependent current-voltage analysis in MATLAB

Numerical analyses of experimental J-V-T data are done to extract parameters such as, ideality factor, series and shunt resistance, saturation current density, and so on, and this is done by fitting a theoretical expression to the experimental data. Knowing that the one-diode model (22) will not be sufficient to fit the whole range of the J-V curve one can either try to fit the experimental data with a two-diode model, much like (19), or fit the two regimes independently. In the work of this thesis, the latter approach was used predominantly. The method used is based on the graphical features of a J-V curve, and thus, for large deviation from ideal double-diode behavior, it will fail.

First, the second derivative of $\log_{10} J(V)$ is calculated. The ideal double-diode would exhibit two linear regimes; thus, the second derivative will be

zero at these two points. The diffusion regime has a steeper slope than the recombination regime, so logically; the first derivative will in the recombination regime have a minimum, and in the diffusion regime a maximum. After applying this logic, the theory of J-V characterization described in chapter 4 can be applied.

A.3 Temperature dependent admittance spectroscopy analysis in MATLAB

Temperature dependent AS numerical analyses follow a similar methodology to J-V analyses. After loading the data in MATLAB, the $\log_{10} C(f)$ function is derivated once, and the maximum derivative found. In the theoretical framework of AS presented in chapter, this may represent the characteristic frequency, ω_o . Subsequent AS analysis is straightforward with the use of the equations in chapter 4. See paper VII and its supplementary information for additional details.

References

- [1] M. Wild, D. Folini, C. Schär, N. Loeb, E. G. Dutton, and G. König-Langlo, "The global energy balance from a surface perspective," *Climate Dynamics*, vol. 40, pp. 3107-3134, 2013.
- [2] IEA, "Key World Energy Statistics," 2016, France.
- [3] M. Holliday, "Testing a Thirty-Year-Old Photovoltaic Module," in *Musings of an Energy Nerd, Contemplating residential energy use* vol. 2010, ed: Green Building Advisor, 2010.
- [4] J. Meydbray and F. Dross, "PV Module Reliability Scorecard Report," DNV GL2016.
- [5] E. Becquerel, "Mémoire sur les effets électriques produits sous l'influence des rayons solaires," *Comptes Rendus*, vol. 9, pp. 561-567, 1839.
- [6] W. G. Adams and R. E. Day, "The Action of Light on Selenium," *Philosophical Transactions of the Royal Society of London*, vol. 167, pp. 313-349, 1877.
- [7] C. E. Fritts, "On a new form of selenium cell, and some electrical discoveries made by its use," *American Journal of Science*, vol. Series 3, vol. 26, pp. 465-472, 1883.
- [8] G. Meyers. (2014). *Photovoltaic Dreaming 1875–1905: First Attempts At Commercializing PV*.
- [9] D. M. Chapin, C. S. Fuller, and G. L. Pearson, "A New Silicon p-n Junction Photocell for Converting Solar Radiation into Electrical Power," *Journal of Applied Physics*, vol. 25, pp. 676-677, 1954.
- [10] "International Technology Roadmap for Photovoltaic Results 2016," 2017.
- [11] "First Solar achieves yet another cell conversion efficiency world record," in *Thin film record 22.1 percent research cell continues performance advancement trend*, S. Krum, Ed., ed: First Solar Inc., 2016.
- [12] "ZSW Sets New World Record for Thin-film Solar Cells," in *CIGS PV's efficiency ratings rising fast*, ed. Stuttgart: Zentrum für Sonnenenergieund Wasserstoff-Forschung Baden-Württemberg, 2016.
- [13] Available: <https://www.nrel.gov/pv/>
- [14] M. A. Green, K. Emery, Y. Hishikawa, W. Warta, and E. D. Dunlop, "Solar cell efficiency tables (version 48)," *Progress in Photovoltaics: Research and Applications*, vol. 24, pp. 905-913, 2016.
- [15] J. Perlin, *Let It Shine: The 6000 Year Story of Solar Energy*. Novato, CA, US: New World Library, 2013.
- [16] A. Chirilă, S. Buecheler, F. Pianezzi, P. Bloesch, C. Gretener, A. R. Uhl, *et al.*, "Highly efficient Cu(In,Ga)Se₂ solar cells grown on flexible polymer films," *Nat Mater*, vol. 10, pp. 857-861, 2011.
- [17] K. P. Bhandari, J. M. Collier, R. J. Ellingson, and D. S. Apul, "Energy payback time (EPBT) and energy return on energy invested (EROI) of solar photovoltaic systems: A systematic review and meta-analysis," *Renewable and Sustainable Energy Reviews*, vol. 47, pp. 133-141, 2015.

- [18] *The Future of Solar Energy: An Interdisciplinary MIT Study*. Massachusetts, USA: Massachusetts Institute of Technology, 2015.
- [19] M. Burgelman, P. Nollet, and S. Degrave, "Modelling polycrystalline semiconductor solar cells," *Thin Solid Films*, vol. 361–362, pp. 527–532, 2000.
- [20] A. Einstein, "Über einen die Erzeugung und Verwandlung des Lichtes betreffenden heuristischen Gesichtspunkt," *Annalen der Physik*, vol. 17, pp. 132–148, 1905.
- [21] U. Malm, "Modelling and Degradation Characteristics of Thin-film CIGS Solar Cells," Ph. D, Engineering Sciences, Uppsala University, Uppsala, 2008.
- [22] S. M. Sze and K. K. Ng, *Physics of Semiconductor Devices*, 3rd ed. United States of America: John Wiley & Sons, 2007.
- [23] W. Shockley and H. J. Queisser, "Detailed Balance Limit of Efficiency of p-n Junction Solar Cells," *Journal of Applied Physics*, vol. 32, pp. 510–519, 1961.
- [24] M. A. Green, *Solar Cells*. Englewood Cliffs, N.J.: Prentice-Hall, Inc., 1982.
- [25] J. Hedstrom, H. Ohlsen, M. Bodegard, A. Kylner, L. Stolt, D. Hariskos, *et al.*, "ZnO/CdS/Cu(In,Ga)Se₂ thin film solar cells with improved performance," in *Conference Record of the Twenty Third IEEE Photovoltaic Specialists Conference - 1993 (Cat. No.93CH3283-9)*, 1993, pp. 364–371.
- [26] P. Jackson, R. Wuerz, D. Hariskos, E. Lotter, W. Witte, and M. Powalla, "Effects of heavy alkali elements in Cu(In,Ga)Se₂ solar cells with efficiencies up to 22.6%," *physica status solidi (RRL) – Rapid Research Letters*, vol. 10, pp. 583–586, 2016.
- [27] A. Chirilă, P. Reinhard, F. Pianezzi, P. Bloesch, A. R. Uhl, C. Fella, *et al.*, "Potassium-induced surface modification of Cu(In,Ga)Se₂ thin films for high-efficiency solar cells," *Nat Mater*, vol. 12, pp. 1107–1111, 2013.
- [28] Y.-T. Hsieh, Q. Han, C. Jiang, T.-B. Song, H. Chen, L. Meng, *et al.*, "Efficiency Enhancement of Cu₂ZnSn(S,Se)₄ Solar Cells via Alkali Metals Doping," *Advanced Energy Materials*, vol. 6, p. 1502386, 2016.
- [29] L. Kronik, D. Cahen, and H. W. Schock, "Effects of Sodium on Polycrystalline Cu(In,Ga)Se₂ and Its Solar Cell Performance," *Advanced Materials*, vol. 10, pp. 31–36, 1998.
- [30] M. Johnson, S. V. Baryshev, E. Thimsen, M. Manno, X. Zhang, I. V. Veryovkin, *et al.*, "Alkali-metal-enhanced grain growth in Cu₂ZnSnS₄ thin films," *Energy & Environmental Science*, vol. 7, pp. 1931–1938, 2014.
- [31] T. Prabhakar and J. Nagaraju, "Alkali assisted enhancement of CZTS absorber layer characteristics," in *2011 37th IEEE Photovoltaic Specialists Conference*, 2011, pp. 001357–001361.
- [32] G. Altamura, M. Wang, and K.-L. Choy, "Influence of alkali metals (Na, Li, Rb) on the performance of electrostatic spray-assisted vapor deposited Cu₂ZnSn(S,Se)₄ solar cells," *Scientific Reports*, vol. 6, p. 22109, 2016.
- [33] P. M. P. Salomé, A. Hultqvist, V. Fjällström, M. Edoff, B. G. Aitken, K. Zhang, *et al.*, "Incorporation of Na in Cu(In,Ga)Se₂ Thin-Film Solar Cells: A Statistical Comparison Between Na From Soda-Lime Glass and From a Precursor Layer of NaF," *IEEE Journal of Photovoltaics*, vol. 4, pp. 1659–1664, 2014.
- [34] A. Hultqvist, P. M. P. Salomé, V. Fjällström, M. Edoff, B. Aitken, K. Zhang, *et al.*, "Performance of Cu(In,Ga)Se₂ solar cells using nominally alkali free glass substrates with varying coefficient of thermal expansion," *Journal of Applied Physics*, vol. 114, p. 094501, 2013.

- [35] N. Naghavi, D. Abou-Ras, N. Allsop, N. Barreau, S. Bücheler, A. Ennaoui, *et al.*, "Buffer layers and transparent conducting oxides for chalcopyrite Cu(In,Ga)(S,Se)₂ based thin film photovoltaics: present status and current developments," *Progress in Photovoltaics: Research and Applications*, vol. 18, pp. 411-433, 2010.
- [36] T. Minemoto, Y. Hashimoto, T. Satoh, T. Negami, H. Takakura, and Y. Hamakawa, "Cu(In,Ga)Se₂ solar cells with controlled conduction band offset of window/Cu(In,Ga)Se₂ layers," *Journal of Applied Physics*, vol. 89, pp. 8327-8330, 2001.
- [37] T. Minemoto, T. Matsui, H. Takakura, Y. Hamakawa, T. Negami, Y. Hashimoto, *et al.*, "Theoretical analysis of the effect of conduction band offset of window/CIS layers on performance of CIS solar cells using device simulation," *Solar Energy Materials and Solar Cells*, vol. 67, pp. 83-88, 2001.
- [38] M. Gloeckler, "Device physics of Cu(In,Ga)Se₂ thin-film solar cells," Ph.D, Department of Physics, Colorado State University, Fort Collins, Colorado, US, 2005.
- [39] J. Lindahl, "Atomic layer deposition of zinc tin oxide buffer layers for Cu(In,Ga)Se₂ solar cells," Ph.D, Engineering Sciences, Uppsala University, Uppsala, 2015.
- [40] J. Keller, L. Stolt, M. Edoff, and T. Törndahl, "Atomic layer deposition of In₂O₃ transparent conductive oxide layers for application in Cu(In,Ga)Se₂ solar cells with different buffer layers," *physica status solidi (a)*, vol. 213, pp. 1541-1552, 2016.
- [41] "Solar Frontier's CIS Thin-Film Submodule Achieves Highest Efficiency World Record of 19.2 %," in *New technology to be applied to mass-produce new solar panels from summer*, ed. Tokyo: Solar Frontier, 2017.
- [42] Q. Cao, O. Gunawan, M. Copel, K. B. Reuter, S. J. Chey, V. R. Deline, *et al.*, "Defects in Cu(In,Ga)Se₂ Chalcopyrite Semiconductors: A Comparative Study of Material Properties, Defect States, and Photovoltaic Performance," *Advanced Energy Materials*, vol. 1, pp. 845-853, 2011.
- [43] J. Lindahl, U. Zimmermann, P. Szaniawski, T. Törndahl, A. Hultqvist, P. Salomé, *et al.*, "Inline Cu(In,Ga)Se₂ Co-evaporation for High-Efficiency Solar Cells and Modules," *IEEE Journal of Photovoltaics*, vol. 3, pp. 1100-1105, 2013.
- [44] U. Rau and H. W. Schock, "Electronic properties of Cu(In,Ga)Se₂ heterojunction solar cells—recent achievements, current understanding, and future challenges," *Applied Physics A*, vol. 69, pp. 131-147, 1999.
- [45] S.-H. Wei, S. B. Zhang, and A. Zunger, "Effects of Ga addition to CuInSe₂ on its electronic, structural, and defect properties," *Applied Physics Letters*, vol. 72, p. 3199, 1998.
- [46] M. I. Alonso, M. Garriga, C. A. Durante Rincón, E. Hernández, and M. León, "Optical functions of chalcopyrite Cu_{Gax}In_{1-x}Se₂ alloys," *Applied Physics A: Materials Science & Processing*, vol. 74, pp. 659-664, 2002.
- [47] B. Shin, O. Gunawan, Y. Zhu, N. A. Bojarczuk, S. J. Chey, and S. Guha, "Thin film solar cell with 8.4% power conversion efficiency using an earth-abundant Cu₂ZnSnS₄ absorber," *Progress in Photovoltaics*, vol. 21, pp. 72-76, 2013.
- [48] T. Ericson, J. J. S. Scragg, A. Hultqvist, J. T. Watjen, P. Szaniawski, T. Törndahl, *et al.*, "Zn(O, S) Buffer Layers and Thickness Variations of CdS Buffer for Cu₂ZnSnS₄ Solar Cells," *IEEE Journal of Photovoltaics*, vol. 4, pp. 465-469, 2014.

- [49] T. Shin, U. Mitsutaro, and M. Takahiro, "Photovoltaic properties of Cu₂ZnSnS₄ cells fabricated using ZnSnO and ZnSnO/CdS buffer layers," *Japanese Journal of Applied Physics*, vol. 55, p. 112302, 2016.
- [50] "Solar Frontier Breaks CZTS Cell Efficiency Record," in *World-record 12.6% cell efficiency achieved with IBM and TOK*, ed. Tokyo, Japan: Solar Frontier, 2012.
- [51] W. Wang, M. T. Winkler, O. Gunawan, T. Gokmen, T. K. Todorov, Y. Zhu, *et al.*, "Device Characteristics of CZTSSe Thin-Film Solar Cells with 12.6% Efficiency," *Advanced Energy Materials*, vol. 4, p. 1301465, 2014.
- [52] K. Sun, C. Yan, F. Liu, J. Huang, F. Zhou, J. A. Stride, *et al.*, "Over 9% Efficient Kesterite Cu₂ZnSnS₄ Solar Cell Fabricated by Using Zn_{1-x}Cd_xS Buffer Layer," *Advanced Energy Materials*, vol. 6, p. 1600046, 2016.
- [53] A. Polizzotti, I. L. Repins, R. Noufi, S. H. Wei, and D. B. Mitzi, "The state and future prospects of kesterite photovoltaics," *Energy & Environmental Science*, vol. 6, pp. 3171-3182, 2013.
- [54] O. Gunawan, T. K. Todorov, and D. B. Mitzi, "Loss mechanisms in hydrazine-processed Cu₂ZnSn(S_e,S)(4) solar cells," *Applied Physics Letters*, vol. 97, p. 233506-1, 2010.
- [55] T. Gokmen, O. Gunawan, T. K. Todorov, and D. B. Mitzi, "Band tailing and efficiency limitation in kesterite solar cells," *Applied Physics Letters*, vol. 103, pp. 103506-1-103506-5, 2013.
- [56] T. Gokmen, O. Gunawan, and D. B. Mitzi, "Semi-empirical device model for Cu₂ZnSn(S_e,S)(4) solar cells," *Applied Physics Letters*, vol. 105, pp. 033903-1-033903-5, 2014.
- [57] S. Siebentritt, "Why are kesterite solar cells not 20% efficient?," *Thin Solid Films*, vol. 535, pp. 1-4, 2013.
- [58] A. Redinger, M. Mousel, M. H. Wolter, N. Valle, and S. Siebentritt, "Influence of S/Se ratio on series resistance and on dominant recombination pathway in Cu₂ZnSn(S_e,S)4 thin film solar cells," *Thin Solid Films*, vol. 535, pp. 291-295, 2013.
- [59] J. K. Larsen, Y. Ren, N. Ross, E. Särhammar, S. Y. Li, and C. Platzer-Björkman, "Surface modification through air annealing Cu₂ZnSn(S_e,S)4 absorbers," *Thin Solid Films*, in press, 2016.
- [60] S. Ahn, S. Jung, J. Gwak, A. Cho, K. Shin, K. Yoon, *et al.*, "Determination of band gap energy (E_g) of Cu₂ZnSnSe₄ thin films: On the discrepancies of reported band gap values," *Applied Physics Letters*, vol. 97, p. 021905, 2010.
- [61] S.-y. Li, S. Zamulko, C. Persson, N. Ross, J. K. Larsen, and C. Platzer-Björkman, "Optical properties of Cu₂ZnSn(S_xSe_{1-x})₄ solar absorbers: Spectroscopic ellipsometry and ab initio calculations," *Applied Physics Letters*, vol. 110, p. 021905, 2017.
- [62] C. Malerba, F. Biccari, C. L. Azanza Ricardo, M. Valentini, R. Chierchia, M. Müller, *et al.*, "CZTS stoichiometry effects on the band gap energy," *Journal of Alloys and Compounds*, vol. 582, pp. 528-534, 2014.
- [63] S.-Y. Li, C. Hägglund, Y. Ren, J. J. S. Scragg, J. K. Larsen, C. Frisk, *et al.*, "Optical properties of reactively sputtered Cu₂ZnSnS₄ solar absorbers determined by spectroscopic ellipsometry and spectrophotometry," *Solar Energy Materials and Solar Cells*, vol. 149, pp. 170-178, 2016.
- [64] K. Neldner, S. Schorr, D. Többers, P. Whitfield, and G. Gurieva, "Phase content and structural analysis of off-stoichiometric Cu₂ZnSnS₄ (CZTS)," presented at the MRS Spring Meeting & Exhibit, San Francisco, US, 2015,
- [65] D. Huang and C. Persson, "Band gap change induced by defect complexes in Cu₂ZnSnS₄," *Thin Solid Films*, vol. 535, pp. 265-269, 2013.

- [66] S. Chen, J.-H. Yang, X. G. Gong, A. Walsh, and S.-H. Wei, "Intrinsic point defects and complexes in the quaternary kesterite semiconductor $\text{Cu}_2\text{ZnSnS}_4$," *Physical Review B*, vol. 81, p. 245204, 2010.
- [67] J. J. S. Scragg, J. K. Larsen, M. Kumar, C. Persson, J. Sendler, S. Siebentritt, *et al.*, "Cu–Zn disorder and band gap fluctuations in $\text{Cu}_2\text{ZnSn}(\text{S},\text{Se})_4$: Theoretical and experimental investigations," *physica status solidi (b)*, vol. 253, pp. 247–254, 2016.
- [68] J. K. Larsen, S.-Y. Li, J. J. S. Scragg, Y. Ren, C. Högglund, M. D. Heinemann, *et al.*, "Interference effects in photoluminescence spectra of $\text{Cu}_2\text{ZnSnS}_4$ and $\text{Cu}(\text{In},\text{Ga})\text{Se}_2$ thin films," *Journal of Applied Physics*, vol. 118, p. 035307, 2015.
- [69] S. Siebentritt and S. Schorr, "Kesterites—a challenging material for solar cells," *Progress in Photovoltaics: Research and Applications*, vol. 20, pp. 512–519, 2012.
- [70] J. J. Scragg, T. Ericson, X. Fontané, V. Izquierdo-Roca, A. Pérez-Rodríguez, T. Kubart, *et al.*, "Rapid annealing of reactively sputtered precursors for $\text{Cu}_2\text{ZnSnS}_4$ solar cells," *Progress in Photovoltaics: Research and Applications*, vol. 22, pp. 10–17, 2014.
- [71] S. Lany and A. Zunger, "Light- and bias-induced metastabilities in $\text{Cu}(\text{In},\text{Ga})\text{Se}_2$ based solar cells caused by the (VSe–VCu) vacancy complex," *Journal of Applied Physics*, vol. 100, p. 113725, 2006.
- [72] A. Urbaniak and M. Igalson, "Creation and relaxation of light- and bias-induced metastabilities in $\text{Cu}(\text{In},\text{Ga})\text{Se}_2$," *Journal of Applied Physics*, vol. 106, p. 063720, 2009.
- [73] V. Fjällström, "Potential-Induced Degradation and possibilities for recovery of $\text{CuIn}_{1-x}\text{Ga}_x\text{Se}_2$ thin film solar cells," Licentiate, Engineering Sciences, Uppsala University, Uppsala, 2015.
- [74] M. Igalson, M. Bodegård, L. Stolt, and A. Jasenek, "The 'defected layer' and the mechanism of the interface-related metastable behavior in the $\text{ZnO}/\text{CdS}/\text{Cu}(\text{In},\text{Ga})\text{Se}_2$ devices," *Thin Solid Films*, vol. 431–432, pp. 153–157, 2003.
- [75] W. Shockley, "The Theory of p-n Junctions in Semiconductors and p-n Junction Transistors," *The Bell System technical journal*, vol. 28, pp. 435–489, 1949.
- [76] J. R. Sites and P. H. Mauk, "Diode Quality Factor Determination for Thin-Film Solar-Cells," *Solar Cells*, vol. 27, pp. 411–417, 1989.
- [77] S. S. Hegedus and W. N. Shafarman, "Thin-film solar cells: Device measurements and analysis," *Progress in Photovoltaics*, vol. 12, pp. 155–176, 2004.
- [78] C. J. Hages, N. J. Carter, R. Agrawal, and T. Unold, "Generalized current-voltage analysis and efficiency limitations in non-ideal solar cells: Case of $\text{Cu}_2\text{ZnSn}(\text{SxSe}_{1-x})_4$ and $\text{Cu}_2\text{Zn}(\text{SnyGe}_{1-y})(\text{SxSe}_{1-x})_4$," *Journal of Applied Physics*, vol. 115, p. 234504, 2014.
- [79] X. X. Liu and J. R. Sites, "Solar-cell collection efficiency and its variation with voltage," *Journal of Applied Physics*, vol. 75, pp. 577–581, 1994.
- [80] S.-Y. Li, "Some optical issues," Å. S. Center, Ed., ed. Uppsala University, 2015.
- [81] K. Decock, "Young Scientist Tutorial: Capacitance Measurements," ed. Spring Meeting Strasbourg, France, 2012.
- [82] T. Walter, R. Herberholz, C. Müller, and H. W. Schock, "Determination of defect distributions from admittance measurements and application to $\text{Cu}(\text{In},\text{Ga})\text{Se}_2$ based heterojunctions," *Journal of Applied Physics*, vol. 80, pp. 4411–4420, 1996.

- [83] K. Decock, S. Khelifi, S. Buecheler, F. Pianezzi, A. N. Tiwari, and M. Burgelman, "Defect distributions in thin film solar cells deduced from admittance measurements under different bias voltages," *Journal of Applied Physics*, vol. 110, pp. 063722-1–063722-12, 2011.
- [84] P. Blood and J. W. Orton, *The electrical characterization of semiconductors: majority carriers and electron states*: Academic Press, 1992.
- [85] D. Mutter and S. T. Dunham, "Calculation of Defect Concentrations and Phase Stability in Cu₂ZnSnS₄ and Cu₂ZnSnSe₄ From Stoichiometry," *IEEE Journal of Photovoltaics*, vol. 5, pp. 1188-1196, 2015.
- [86] L. C. Kimerlin, "Influence of Deep Traps on Measurement of Free-Carrier Distributions in Semiconductors by Junction Capacitance Techniques," *Journal of Applied Physics*, vol. 45, pp. 1839–1845, 1974.
- [87] A. Niemegeers and M. Burgelman, "Numerical modelling of AC-characteristics of CdTe and CIS solar cells," in *Conference Record of the Twenty Fifth IEEE Photovoltaic Specialists Conference - 1996*, 1996, pp. 901-904.
- [88] S. Degraeve, M. Burgelman, and P. Nollet, "Modelling of polycrystalline thin film solar cells: new features in SCAPS version 2.3," in *3rd World Conference on Photovoltaic Energy Conversion, 2003. Proceedings of*, 2003, pp. 487-490 Vol.1.
- [89] J. Verschraegen and M. Burgelman, "Numerical modeling of intra-band tunneling for heterojunction solar cells in scaps," *Thin Solid Films*, vol. 515, pp. 6276-6279, 2007.
- [90] K. Decock, J. Lauwaert, and M. Burgelman, "Characterization of graded CIGS solar cells," *Energy Procedia*, vol. 2, pp. 49–54, 2010.
- [91] K. Decock, S. Khelifi, and M. Burgelman, "Modelling multivalent defects in thin film solar cells," *Thin Solid Films*, vol. 519, pp. 7481-7484, 2011.
- [92] M. Burgelman, K. Decock, S. Khelifi, and A. Abass, "Advanced electrical simulation of thin film solar cells," *Thin Solid Films*, vol. 535, pp. 296–301, 2013.
- [93] K. Decock, P. Zabierowski, and M. Burgelman, "Modeling metastabilities in chalcopyrite-based thin film solar cells," *Journal of Applied Physics*, vol. 111, p. 043703, 2012.
- [94] J. Pettersson, "Modelling Band Gap Gradients and Cd-free Buffer Layers in Cu(In,Ga)Se₂ Solar Cells," Ph.D., Engineering Sciences, Uppsala University, Uppsala, 2012.
- [95] T. Dullweber, G. Hanna, W. Shams-Kolaji, A. Schwartzlander, M. A. Contreas, R. Noufi, *et al.*, "Study of the effect of gallium grading in Cu(In,Ga)Se₂," *Thin Solid Films*, vol. 361-362, pp. 478-481, 2000.
- [96] J. Song, S. S. Li, C. H. Huang, O. D. Crisalle, and T. J. Anderson, "Device modeling and simulation of the performance of Cu(In_{1-x}Ga_x)Se₂ solar cells," *Solid-State Electronics*, vol. 48, pp. 73-79, 2004.
- [97] Y. Hirai, Y. Kurokawa, and A. Yamada, "Numerical study of Cu(In,Ga)Se₂ solar cell performance toward 23% conversion efficiency," *Japanese Journal of Applied Physics*, vol. 53, p. 012301, 2014.
- [98] M. Topič, F. Smole, and J. Furlan, "Band-gap engineering in CdS/Cu(In,Ga)Se₂ solar cells," *Journal of Applied Physics*, vol. 79, p. 8537, 1996.
- [99] M. Gloeckler and J. R. Sites, "Band-gap grading in Cu(In,Ga)Se₂ solar cells," *Journal of Physics and Chemistry of Solids*, vol. 66, pp. 1891–1894, 2005.
- [100] G. Hanna, A. Jasenek, U. Rau, and H. W. Schock, "Influence of the Ga-content on the bulk defect densities of Cu(In,Ga)Se₂," *Thin Solid Films*, vol. 287, pp. 71-73, 2001.

- [101] P. Jackson, D. Hariskos, E. Lotter, S. Paetel, R. Wuerz, R. Menner, *et al.*, "New world record efficiency for Cu(In,Ga)Se₂ thin-film solar cells beyond 20%," *Progress in Photovoltaics: Research and Applications*, vol. 19, pp. 894-897, 2011.
- [102] D. Kuciauskas, J. V. Li, M. A. Contreras, J. Pankow, P. Dippo, M. Young, *et al.*, "Charge carrier dynamics and recombination in graded band gap CuIn_{1-x}Ga_xSe₂ polycrystalline thin-film photovoltaic solar cell absorbers," *Journal of Applied Physics*, vol. 114, p. 154505, 2013.
- [103] B. Vermang, V. Fjällström, J. Pettersson, P. Salomé, and M. Edoff, "Development of rear surface passivated Cu(In,Ga)Se₂ thin film solar cells with nano-sized local rear point contacts," *Solar Energy Materials and Solar Cells*, vol. 117, pp. 505-511, 2013.
- [104] S. Levchenko, G. Gurieva, M. Guc, and A. Nateprov, "Optical constants of Cu₂ZnSnS₄ bulk crystals," *Moldavian Journal of the Physical Sciences*, vol. 8, pp. 173-177, 2009.
- [105] J. P. Leita, N. M. Santos, P. A. Fernandes, P. M. P. Salome, A. F. da Cunha, J. C. Gonzalez, *et al.*, "Study of optical and structural properties of Cu₂ZnSnS₄ thin films," *Thin Solid Films*, vol. 519, pp. 7390-7393, 2011.
- [106] C. Persson, "Electronic and optical properties of Cu₂ZnSnS₄ and Cu₂ZnSnSe₄," *Journal of Applied Physics*, vol. 107, pp. 053710-1-053710-8, 2010.
- [107] U. Rau and J. H. Werner, "Radiative efficiency limits of solar cells with lateral band-gap fluctuations," *Applied Physics Letters*, vol. 84, pp. 3735-3737, 2004.
- [108] S. Chen, X. G. Gong, A. Walsh, and S.-H. Wei, "Electronic structure and stability of quaternary chalcogenide semiconductors derived from cation cross-substitution of II-VI and I-III-VI₂ compounds," *Physical Review B*, vol. 79, p. 165211, 2009.
- [109] S. Chen, A. Walsh, J.-H. Yang, X. G. Gong, L. Sun, P.-X. Yang, *et al.*, "Compositional dependence of structural and electronic properties of Cu₂ZnSn(S,Se)₄ alloys for thin film solar cells," *Physical Review B*, vol. 83, p. 125201, 2011.
- [110] S. Adachi, "Physical Properties: Compiled Experimental Data," in *Copper Zinc Tin Sulfide-Based Thin Film Solar Cells*, K. Ito, Ed., ed Nagano, Japan: John Wiley & Sons Ltd., 2015.
- [111] N. Ross, J. Larsen, S. Grini, L. Vines, and C. Platzer-Björkman, "Practical limitations to selenium annealing of compound co-sputtered Cu₂ZnSnS₄ as a route to achieving sulfur-selenium graded solar cell absorbers," *Thin Solid Films*, vol. 623, pp. 110-115, 2017.

Acta Universitatis Upsaliensis

*Digital Comprehensive Summaries of Uppsala Dissertations
from the Faculty of Science and Technology 1514*

Editor: The Dean of the Faculty of Science and Technology

A doctoral dissertation from the Faculty of Science and Technology, Uppsala University, is usually a summary of a number of papers. A few copies of the complete dissertation are kept at major Swedish research libraries, while the summary alone is distributed internationally through the series Digital Comprehensive Summaries of Uppsala Dissertations from the Faculty of Science and Technology. (Prior to January, 2005, the series was published under the title "Comprehensive Summaries of Uppsala Dissertations from the Faculty of Science and Technology".)

Distribution: publications.uu.se
urn:nbn:se:uu:diva-320308



ACTA
UNIVERSITATIS
UPSALIENSIS
UPPSALA
2017